

Nonlinear equilibrium solutions in a three-dimensional boundary layer and their secondary instability

By WERNER KOCH, FABIO P. BERTOLOTTI[†],
ANDREAS STOLTE[‡] AND STEFAN HEIN

DLR Institut für Strömungsmechanik, D-37073 Göttingen, Germany

(Received 23 November 1998 and in revised form 22 October 1999)

The observed nonlinear saturation of crossflow vortices in the DLR swept-plate transition experiment, followed by the onset of high-frequency signals, motivated us to compute nonlinear equilibrium solutions for this flow and investigate their instability to high-frequency disturbances. The equilibrium solutions are independent of receptivity, i.e. the way crossflow vortices are generated, and thus provide a unique characterization of the nonlinear flow prior to turbulence. Comparisons of these equilibrium solutions with experimental measurements exhibit strong similarities. Additional comparisons with results from the nonlinear parabolized stability equations (PSE) and spatial direct numerical simulations (DNS) reveal that the equilibrium solutions become unstable to steady, spatial oscillations with very long wavelengths following a bifurcation close to the leading edge. Such spatially oscillating solutions have been observed also in critical layer theory computations. The nature of the spatial behaviour is herein clarified and shown to be analogous to that encountered in temporal direct numerical simulations. We then employ Floquet theory to systematically study the dependence of the secondary, high-frequency instabilities on the saturation amplitude of the equilibrium solutions. With increasing amplitude, the most amplified instability mode can be clearly traced to *spanwise* inflectional shear layers that occur in the wake-like portions of the equilibrium solutions (Malik *et al.* 1994 call it ‘mode I’ instability). Both the frequency range and the eigenfunctions resemble recent experimental measurements of Kawakami *et al.* (1999). However, the lack of an explosive growth leads us to believe that additional self-sustaining processes are active at transition, including the possibility of an absolute instability of the high-frequency disturbances.

1. Introduction

The early history of laminar–turbulent transition on swept wings is full of excitement and lessons learned from failures. A description can be found in the review papers of Reed & Saric (1989), Arnal (1992), Saric (1992), Reed, Saric & Arnal (1996), Malik (1997) or Bippes (1999), which contain also most of the relevant references. At the cruise conditions of modern jet aircraft the atmospheric turbulence level is very low, leaving surface roughness as the major source of disturbance generation. The steady disturbances, known as crossflow vortices, rapidly grow in the region of

[†] Present address: United Technologies Research Center, East Hartford, CT 06108, USA.

[‡] Present address: PSI AG, D-10178 Berlin, Germany.

accelerated flow between the attachment line and the location of peak suction on the airfoil. Their initial exponential growth is followed by nonlinear saturation once the amplitude reaches levels of the order of 10% to 30% of the free-stream velocity. This saturation can be clearly seen in experiments that simulate the essential features of three-dimensional flow over swept wings, such as the DLR infinite-swept-plate experiment, cf. Bippes (1999). Since the crossflow disturbances saturate in amplitude, it is natural to ask if the saturation states are equilibrium solutions of the flow. In this paper we show that equilibrium solutions exist in the three-dimensional boundary layer of the DLR experiment, and that certain features of the equilibrium solutions resemble those measured in the experiment. If the saturation states are indeed equilibrium solutions, our current methodology of transition prediction would have to be modified, since the flow would reach the equilibrium solutions independently of the location and strength of the crossflow mode generation, making predictions based on the magnitude of the disturbance growth, such as the popular e^N methods, completely irrelevant.

By comparing our equilibrium solution for steady crossflow vortices with the saturation states of spatial direct numerical simulations as well as parabolized stability equation (PSE) computations, we find that the amplitudes of the saturation states seem to approach the equilibrium solution but do not follow it further downstream. We trace the reason for this deviation to a bifurcation near the leading edge that makes the equilibrium solution unstable to steady, spatial oscillations with very long wavelengths of the order of the chord length of the DLR plate. The spatially stable branch is represented by the spatially oscillating solutions of spatial direct numerical simulations (DNS), PSE or critical layer theory. However, at peak amplitude the PSE solution and the equilibrium solution remain similar to each other, making the equilibrium solution and its characteristics a relevant, receptivity-independent, nonlinear base flow model for investigating the nonlinear stages of transition leading to breakdown into turbulence. In particular, the equilibrium solution appears to provide something like an envelope of the maximal saturation amplitudes of steady crossflow vortices as a function of chord position and spanwise wavenumber.

Additionally, the present work is concerned with the stability of the equilibrium solution to high-frequency disturbances. Findings in this area help our understanding of the nonlinear mechanisms leading to breakdown in three-dimensional boundary layers. We use the clear relationship between amplitude, wavenumber, and chord location of the equilibrium solution to investigate the dependence of high-frequency secondary instabilities on the amplitude of the crossflow vortices. Such high-frequency instabilities have been observed in several experiments shortly before breakdown, cf. Arnal, Coustols & Juillen (1984), Poll (1985), Michel, Arnal & Juillen (1985), Kohama, Saric & Hoos (1991), Kohama, Onondera & Egami (1996) or Lerche (1997). High-frequency instabilities due to internal high-shear layers appear to be a generic indicator of an imminent breakdown, see for example the review by Tani (1980), and play an important role in the conjectured self-sustaining process in shear flows of Waleffe (1997). They have also been observed in a two-dimensional Blasius boundary layer, where they are generally associated with the ‘spike stage’ (cf. the experiments of Klebanoff, Tidstrom & Sargent (1962) or Nishioka, Asai & Iida (1980) for fundamental breakdown, Bake, Kachanov & Fernholz (1996) for subharmonic breakdown, and Wiegel (1997) or Berlin, Wiegel & Henningson (1999) for oblique breakdown). However, usually in a Blasius boundary layer low-frequency three-dimensional secondary instabilities with initially very high growth rates, cf. the discussion in Herbert & Morkovin (1980) or Herbert (1988), have

to pave the way for the now tertiary high-frequency instability. Contrary to this, high-frequency instabilities in a three-dimensional boundary layer already occur as secondary instabilities of crossflow vortices. So, even though the base flow is more complicated, the physical process is more apparent in a three-dimensional boundary layer, because here secondary instability causes the first appearance of high-frequency small-scale disturbances. Closely related problems, such as the secondary instability of Görtler vortices, cf. Park & Huerre (1995), Li & Malik (1995) or Bottaro & Klingmann (1996) or, bypassing the primary instability, the secondary instability of streaks in a Blasius boundary layer, cf. the forthcoming paper by Andersson *et al.* (1999), display very similar mechanisms of breakdown.

1.1. Secondary instability approaches

Following the successful explanation of the onset of three-dimensionality in two-dimensional shear flows and boundary layers via secondary instability theory, cf. Herbert (1984, 1988), it was only natural to apply secondary stability analysis also to three-dimensional boundary layers. In a two-dimensional boundary layer the low threshold amplitude for secondary instabilities allows the application of the simplifying ‘shape assumption’, which neglects the nonlinear distortion of the primary wave. This simplification is no longer justified for three-dimensional boundary layers where high primary amplitudes are observed before the occurrence of secondary instabilities. Nevertheless, practically all early secondary instability investigations, cf. Reed (1984, 1988), Fischer & Dallmann (1987, 1991) invoked this simplification in the hope of obtaining at least qualitatively correct results. For the primary, stationary crossflow vortices of the DLR swept-plate experiment only *low-frequency* secondary instabilities were obtained, see Fischer & Dallmann (1987, 1991), unless the amplitude of the primary vortex was increased to very high values, cf. Fischer, Hein & Dallmann (1993). According to Högberg & Henningson (1998) these low-frequency secondary instabilities correspond to travelling primary crossflow vortices which interact nonlinearly with the stationary crossflow vortices, clearly visible for example in the temporal direct numerical simulation (DNS) of Wintergerste & Kleiser (1997). A major effect of this nonlinear interaction with travelling crossflow vortices is the reduction of the saturation amplitude as exemplified by the experiments of Deyhle & Bippes (1996) or the parabolized stability equation (PSE) results of Malik, Li & Chang (1994) or Bertolotti (1996).

That inflectional shear layers are at the root of high-frequency instabilities has been pointed out for plane Poiseuille flow by Nishioka *et al.* (1980). In the context of crossflow vortices the importance of inflectional shear layers for the *high-frequency* secondary instabilities was first suggested by the temporal DNS of Malik (1986) for the boundary layer on a rotating disk, or of Meyer & Kleiser (1988) for the boundary layer in the DLR swept-plate experiment. It has been demonstrated also for other three-dimensional boundary layers by the nonlinear PSE computations of Malik & Li (1992), Malik *et al.* (1994) and Malik, Li & Chang (1996). The simple *ad hoc* primary stability calculations for the nonlinearly deformed mean flow profiles obtained by a temporal DNS, cf. Wagner (1992), or recently by a PSE approach, cf. Copie (1996), underscore the importance of inflectional shear layers, but the correct approach is via secondary instability theory. Using the rotating-disk model flow Balachandar, Streett & Malik (1992) were the first to theoretically study high-frequency secondary instability of stationary crossflow vortices and obtained results very similar to those observed in the experiment of Kohama (1984, 1987). Based on the result that this instability occurs at high vortex amplitudes, Balachandar *et al.* (1992) realised

the importance of the mean flow distortion and made substantial theoretical and computational contributions to the subject of high-frequency secondary instability. In particular they pointed out that in order to resolve the thin shear layers of the nonlinearly deformed primary flow many more Floquet modes are necessary than for two-dimensional boundary layers.

The rotating disk problem with its self-similar exact solution for the steady laminar flow is a frequently studied model problem for three-dimensional boundary layers, cf. for example Gregory, Stuart & Walker (1955), Malik, Wilkinson & Orszag (1981) or Kohama (1984). However, despite the often invoked analogy between the rotating-disk boundary layer and the boundary layer on a swept wing there exist deep-rooted differences. Namely, Lingwood (1995, 1996) showed that the boundary layer on the rotating disk is absolutely unstable while the boundary layer on a swept wing is, as far as we know, convectively unstable, cf. Lingwood (1997), Taylor & Peake (1998) or Turkyilmazoglu & Gajjar (1999). This not only indicates the possibility of chordwise and spanwise contamination in the swept-wing problem, but also suggests the existence of different transition mechanisms.

For the technologically more interesting swept-wing flow no exact solutions of the laminar flow exist and non-similar, three-dimensional boundary layer solutions have to be computed numerically. Nevertheless, most investigators use simpler model flows allowing similarity approximations for the laminar base flow, such as swept Hiemenz or Falkner–Skan–Cooke flow, to gain more insight into swept-wing transition. The nonlinearly deformed primary base flow for the high-frequency secondary stability analysis is then obtained by temporal or spatial DNS, or nonlinear parabolized equations similar to those introduced by the pioneering work of Hall (1983). In the present paper we use a third possibility, namely nonlinear temporal equilibrium solutions. While the latter together with temporal DNS are basically local analyses, spatial DNS and nonlinear PSE include non-local effects by taking into account non-parallel boundary-layer changes.

High-frequency secondary stability computations for *swept Hiemenz flow* have been reported by Malik & Li (1993), Malik *et al.* (1994), Wang, Herbert & Stuckert (1994) and Janke & Balakumar (1998a). All authors used nonlinear PSE solutions as base flow for their temporal secondary stability analysis. They demonstrate that many Floquet modes have to be retained in order to obtain convergence, resulting in very large matrix eigenvalue problems. As a consequence Janke & Balakumar (1998a) applied the recently developed implicitly restarted Arnoldi method instead of the classical QZ-algorithm to solve the global eigenvalue problem. Unstable high-frequency secondary eigenvalues were observed only at higher amplitudes of the steady crossflow vortices. Malik *et al.* (1994) identified several unstable eigenvalues for high enough crossflow amplitude but discussed only one eigenfunction in more detail. Contrary to the low-frequency secondary eigenfunctions, this high-frequency secondary eigenfunction reached its maximum amplitude near the boundary-layer edge at the top of the stationary crossflow vortex. In the follow-up paper Malik *et al.* (1996) applied their two-dimensional eigenvalue approach to the swept-wing experiment of Kohama *et al.* (1991) as well as to the swept cylinder experiment of Poll (1985). They identified two types of high-frequency secondary modes, one correlating with spanwise shear and the other with vertical shear. This is similar to secondary instability results for Görtler vortices, cf. Park & Huerre (1995), Li & Malik (1995) or Bottaro & Klingmann (1996), where these two modes are referred to as sinuous and varicose (horse-shoe) modes.

Högberg & Henningson (1998) used spatial DNS to compute stationary crossflow

vortices for the *DLR swept-plate experiment* before adding small random disturbances numerically at various locations. The authors took the laminar flow to be a self-similar Falkner–Skan–Cooke boundary layer and found low- and high-frequency secondary instabilities. Again the high-frequency instability could only be excited if the stationary vortex was nearly saturated. They found the growth rate of the high-frequency secondary disturbance to be considerably higher than the growth rate of the low-frequency secondary disturbance, emphasizing the importance of high-frequency secondary instabilities for the transition process.

Recently Janke & Balakumar (1998*a*), see also Janke (1998), published secondary stability results for swept Hiemenz flow as well as for the DLR swept-plate experiment. Using a non-similar base flow together with nonlinear PSE they even demonstrated the existence of a modal coincidence, which they called erroneously an absolute instability. Modal coincidence is a necessary condition for absolute instability but not sufficient. Unless the ‘pinching’ condition of Briggs (1964), cf. the extension to spatially periodic flows by Brevdo & Bridges (1996), is also satisfied, a local degeneracy of the dispersion relation merely indicates the coincidence of waves propagating in the same direction. In their forthcoming publication Janke & Balakumar (1998*b*) therefore corrected their statement about absolute instability. Nevertheless, the resulting locally algebraic growth could be a possible transition mechanism. But the apparent existence of many such degeneracies (also between slightly damped modes) makes it rather difficult to decide which of these could be relevant for transition. On the other hand, the wake-like profiles of the streamwise vortex velocity plausibly suggest that an absolute instability of secondary instability modes satisfying the pinching criterion might exist and be the self-sustaining process causing breakdown. This hypothesis is at present still under investigation.

The results cited above provide a detailed description of secondary instability in boundary-layer flows for specific flow conditions. Most studies employed nonlinear PSE solutions as base flow and therefore are sensitive to initial conditions due to the spatial Hopf bifurcation in the flow. As an undesirable consequence of this fact, the initial conditions enter as an extra parameter in the problem. The experimental results of Deyhle & Bippes (1996) also show that the initial conditions, given by the disturbance environment, influence the transition in a rather intricate way. The use of equilibrium solutions removes the initial conditions as a parameter from the problem and allows one to search for general stability properties of the swept-plate boundary layer.

In §§ 2 and 3 we describe the laminar flow and compute equilibrium solutions for stationary or travelling crossflow vortices relevant to the parameters of the DLR swept-plate experiment. The case where both stationary and travelling crossflow vortices interact is more difficult, because the resulting flow is no longer Galilei invariant under the parallel flow assumption, and is not treated herein. The swept-plate experiment has been conducted in Göttingen by Bippes and his group, cf. for example Nitschke-Kowsky & Bippes (1988), Müller & Bippes (1988), Bippes, Müller & Wagner (1991), Deyhle, Höhler & Bippes (1993) or Deyhle & Bippes (1996), as a basic experiment and data base for crossflow instability and transition research in a three-dimensional boundary layer without the influence of body curvature. Comparing the equilibrium solution with the PSE results for various initial conditions, we clarify the bifurcation behaviour into the spatially oscillating quasi-equilibria of the PSE solutions. Using particular scalings such periodic or pseudo-periodic solutions were also observed as possible solutions of amplitude equations in unsteady critical layer theory, cf. Smith, Brown & Brown (1993), Gajjar (1996) or Brown & Smith (1996). In § 4, we describe

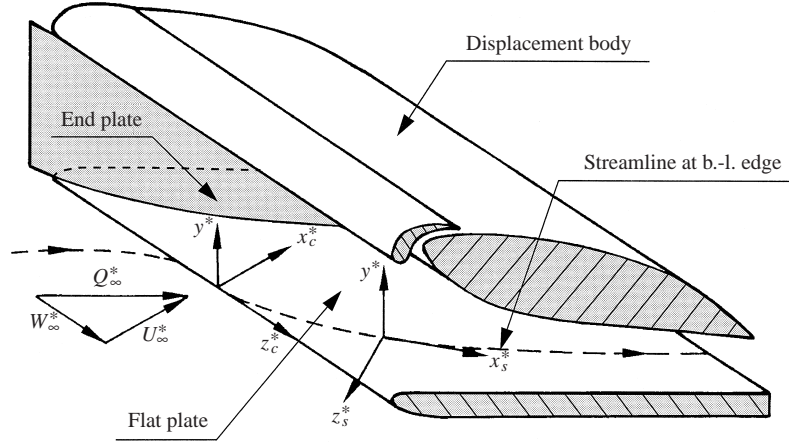


FIGURE 1. DLR infinite-swept-plate experiment, cf. Bippes *et al.* (1991).

the governing equations for secondary instability, and present results for our nonlinear equilibrium flow created by stationary crossflow vortices which is most relevant to the low-disturbance environment of free flight. Following a detailed analysis, we identify the mode that can be expected to play an important role in the breakdown process.

2. Laminar base flow

2.1. Infinite-swept-plate potential flow

In the following we shall consider the incompressible flow over an infinite swept flat plate with an imposed favourable pressure gradient (i.e. decreasing pressure in the chord direction). This model flow, specifically designed for the study of crossflow instabilities without the influence of body curvature, has the advantage that several experimental results exist for comparison, cf. the recent survey by Bippes (1999). In particular we choose our parameters within the range of the DLR swept-plate experiment, sketched in figure 1, which has frequently been used as a data base for temporal DNS, cf. Meyer & Kleiser (1988) or Meyer (1989), spatial DNS, cf. Joslin & Streett (1994), Müller (1995) or Müller, Bestek & Fasel (1995) and PSE computations, cf. Bertolotti (1996) or Janke & Balakumar (1998a). In the DLR experiment the favourable, essentially constant, negative pressure gradient in the direction normal to the leading edge is induced by a displacement body above the plate. Contoured end plates, aligned with the streamlines at the boundary-layer edge, approximate infinite swept plate conditions with a geometric sweep angle of 45° which, due to the displacement effect of the wind tunnel model, is reduced to an effective sweep angle of $\varphi_\infty = 42.5^\circ$. The chord length of the plate c^* is 0.5 m and the dimensional free-stream velocity Q_∞^* equals 19 m s^{-1} (dimensional quantities are denoted by an asterisk).

All velocities $\mathbf{q}^* = (u^*, v^*, w^*)$ are decomposed into the (steady) laminar base flow $\mathbf{Q}^* = (U^*, V^*, W^*)$, denoted by upper-case letters, and the (fluctuating) disturbance velocities $\tilde{\mathbf{q}}^* = (\tilde{u}^*, \tilde{v}^*, \tilde{w}^*)$

$$\mathbf{q}^*(x^*, y^*, z^*, t^*) = \mathbf{Q}^*(x^*, y^*, z^*) + \varepsilon_p \tilde{\mathbf{q}}^*(x^*, y^*, z^*, t^*). \quad (2.1)$$

Here the primary amplitude ε_p has been introduced for convenient comparison with linear and weakly nonlinear results. But in our case ε_p can be arbitrarily large and

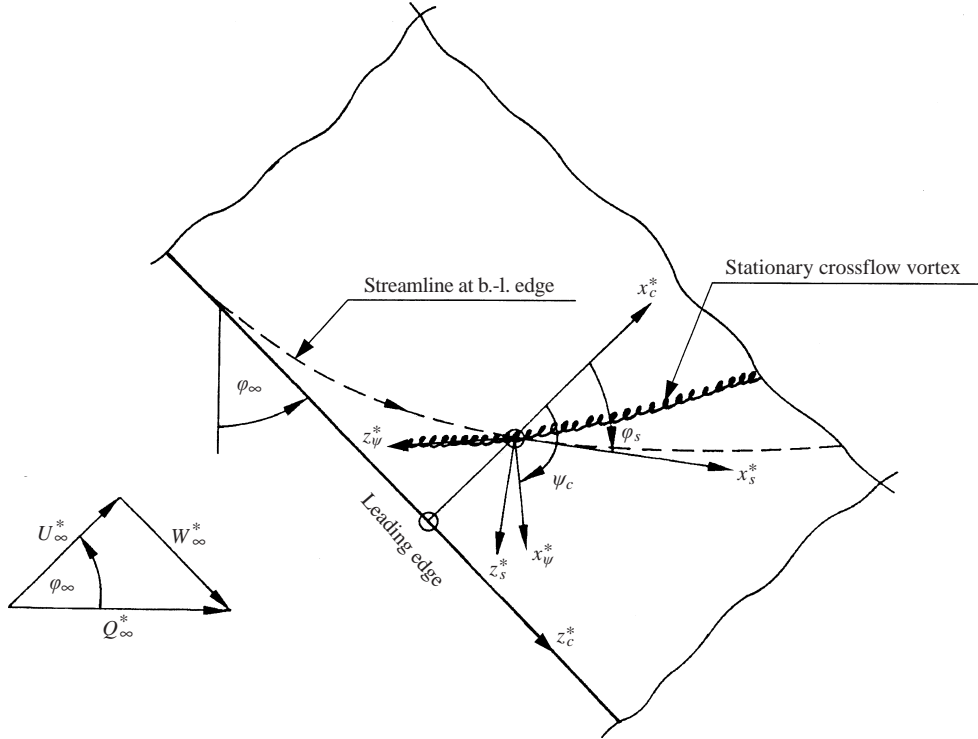


FIGURE 2. Infinite swept plate: coordinate systems.

will be quantified in our continuation procedure by a normalization condition. We define a body-fixed, *chordwise coordinate system* (x_c^*, y^*, z_c^*) , denoted by the subscript c , where x_c^* is in the chordwise direction, z_c^* is in the spanwise direction, and y^* is normal to the plate. The corresponding velocities are denoted by (u_c^*, v^*, w_c^*) . For the primary instability analysis it is customary to introduce a local *streamwise coordinate system* (x_s^*, y^*, z_s^*) , denoted by the subscript s , where x_s^* is in the direction of the local free-stream velocity $U_{s,e}^*$ at the boundary-layer edge, and z_s^* is in the crossflow direction normal to x_s^* . Figure 2 shows the various coordinate systems, including the *wave-oriented coordinate system* $(x_\psi^*, y^*, z_\psi^*)$ to be used in the stability analysis.

Due to the infinite-swept-wing assumption the spanwise velocity $W_{c,e}^* = Q_\infty^* \sin \varphi_\infty$ at the edge of the boundary layer is constant and the chordwise velocity $U_{c,e}^* = Q_\infty^* \cos \varphi_\infty (1 - c_p)^{1/2}$ at the boundary-layer edge depends only on x_c^* . For a given wall pressure coefficient $c_p(x_c^*) = (p^*(x_c^*) - p_\infty^*) / (\rho^* U_{c,\infty}^{*2} / 2)$ the local potential velocity at the boundary-layer edge can then be expressed in terms of c_p

$$Q_e^*(x_c^*) = \{(U_{c,e}^*)^2 + (W_{c,e}^*)^2\}^{1/2} = Q_\infty^* \{(1 - c_p) \cos^2 \varphi_\infty + \sin^2 \varphi_\infty\}^{1/2}, \quad (2.2)$$

with the corresponding local sweep angle

$$\varphi_s(x_c^*) = \arctan(W_{c,e}^*/U_{c,e}^*) = \arctan\{\tan \varphi_\infty / (1 - c_p)^{1/2}\}. \quad (2.3)$$

Meyer (1989) used a least-squares fit to approximate the experimentally measured pressure coefficient $c_p(x_c^*)$ for $x_c^* > 0.04c^*$ analytically by the linear function

$$c_p(x_c^*/c^*) = 0.941 - 0.845(x_c^*/c^*)$$

which was also used by amongst others Joslin & Streett (1994) or Müller (1995). For

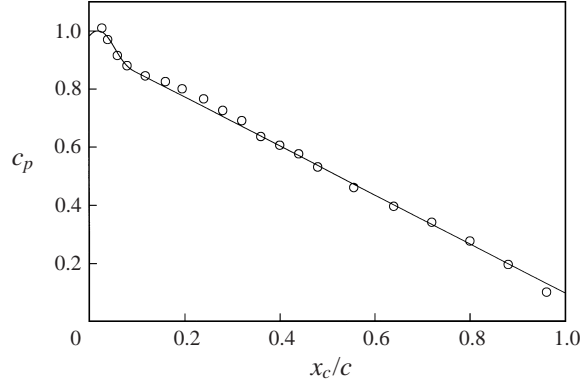


FIGURE 3. Experimental pressure distribution (○) on the DLR swept plate (Müller & Bippes 1988) together with analytical approximation (2.4).

the non-similar boundary-layer computation used in our analysis it is necessary to include the stagnation point and we therefore supplemented the above approximation for $x_c^*/c^* < 0.1$ as follows:

$$c_p = \begin{cases} a_1(x_c^*/c^* - 0.02)^2 + a_0: & x_c^*/c^* \leq 0.04, \\ b_4(x_c^*/c^*)^4 + b_3(x_c^*/c^*)^3 + b_2(x_c^*/c^*)^2 + b_1(x_c^*/c^*) + b_0: & 0.04 < x_c^*/c^* \leq 0.1, \\ 0.941 - 0.845(x_c^*/c^*): & 0.1 < x_c^*/c^*. \end{cases} \quad (2.4)$$

The coefficients

$$a_0 = 1.0, \quad a_1 = -53.7045,$$

$$b_0 = 0.852153, \quad b_1 = 12.2960, \quad b_2 = -340.922, \quad b_3 = 3231.52, \quad b_4 = -10475.6$$

were chosen such that the pressure coefficient is continuous up to second order and approximates the experimental values of Müller & Bippes (1988) with a stagnation point at $x_c^*/c^* = 0.02$, cf. figure 3.

2.2. Infinite-swept-plate boundary layer

Instead of solving the rather complicated Navier–Stokes boundary-value problem for the laminar flow over the swept plate depicted in figure 1, we solve the boundary-layer equations for an infinite swept plate subject to the edge velocity (2.2) in conjunction with (2.4). Following standard practice, e.g. White (1974), we introduce the coordinate system (x_c, χ, z_c) , where x_c and z_c are the chordwise and spanwise coordinates non-dimensionalized with a fixed global reference length such as the plate chord c^* . The local similarity variable χ is defined by

$$\chi = y^*/\delta^*(x_c^*) \quad \text{with} \quad \delta^*(x_c^*) = \sqrt{\nu^* x_c^*/U_{c,e}^*(x_c^*)}, \quad (2.5)$$

where ν^* denotes the kinematic viscosity. Then the boundary-layer equations can be written in terms of the stream function $\Psi^*(x_c, \chi)$ and spanwise velocity $W_c^*(x_c, \chi)$

$$\Psi^*(x_c, \chi) = \sqrt{U_{c,e}^*(x_c^*)\nu^*x_c^*} F(x_c, \chi), \quad (2.6)$$

$$W^*(x_c, \chi) = W_{c,e}^* G(x_c, \chi), \quad (2.7)$$

such that

$$F''' + \frac{1}{2 - \beta_H} F F'' + \frac{\beta_H}{2 - \beta_H} \{1 - F'^2\} + x_c \left(F'' \frac{\partial F}{\partial x_c} - F' \frac{\partial F'}{\partial x_c} \right) = 0, \quad (2.8)$$

$$G'' + \frac{1}{2 - \beta_H} F G' + x_c \left(G' \frac{\partial F}{\partial x_c} - F' \frac{\partial G}{\partial x_c} \right) = 0. \quad (2.9)$$

Here primes denote differentiation with respect to χ , and F and G satisfy the boundary conditions

$$\begin{aligned} F(x_c, \chi) = F'(x_c, \chi) = G(x_c, \chi) = 0, \quad \chi = 0, \\ F'(x_c, \chi) = G(x_c, \chi) = 1, \quad \chi \rightarrow \infty. \end{aligned}$$

The term β_H is the Hartree pressure-gradient parameter, defined as

$$\beta_H = \left(\frac{1}{2} - \frac{1 - c_p}{x_c^* (dc_p/dx_c^*)} \right)^{-1}. \quad (2.10)$$

Without the x_c -derivatives, equations (2.8), (2.9) reduce to the frequently used *Falkner–Skan–Cooke* equations for self-similar boundary layers. We solve the non-similar equations (2.8), (2.9) starting from the stagnation point, where the velocities are computed via Hiemenz equations, and march downstream using an accurate spectral multi-domain code employing a first-order Euler discretization of the x_c derivatives.

2.3. Local reference quantities

For the following analysis we introduce local reference quantities at each chordwise location $x_c^* = x_{c,r}^*$ under investigation. In particular we take the similarity length $\delta^*(x_{c,r}^*)$, defined in equation (2.5), as local reference length $L_{ref}^* = \{v^* x_{c,r}^* / U_{c,e}^*(x_{c,r}^*)\}^{1/2}$, such that our dimensionless coordinates are $x = x^* / L_{ref}^*$, $y = y^* / L_{ref}^* = \chi(x_{c,r}^*)$, $z = z^* / L_{ref}^*$. The use of the reference length $\delta^*(x_{c,r}^*)$ offers the numerical advantage that the boundary layer occupies roughly the same portion of the computational domain independent of chordwise position. Our reference velocity is the local free-stream velocity (2.2), i.e. $Q_{ref}^* = Q_e^*(x_{c,r}^*)$. Then the local Reynolds number is defined by

$$Re = Q_{ref}^* L_{ref}^* / v^* = \{U_{c,e}^*(x_{c,r}^*) x_{c,r}^* / v^*\}^{1/2} / \cos \varphi_s(x_{c,r}^*). \quad (2.11)$$

The normal boundary-layer velocity V is of higher order in terms of the local Reynolds number and will be neglected in our equilibrium solution. Furthermore, we assume that locally the laminar base flow depends only on y (*quasi-parallel boundary layer*) such that

$$\mathbf{Q}_c(x_c, y, z_c) \equiv (U_c(y), 0, W_c(y)) = (F'(x_c; y) \cos \varphi_s, 0, G(x_c; y) \sin \varphi_s) \quad (2.12)$$

is our quasi-parallel laminar base flow in chordwise coordinates. Figure 4 depicts the streamwise and crossflow velocities U_s and W_s , defined by

$$U_s(y) = U_s^* / Q_e^* = F'(x_c; y) \cos^2 \varphi_s + G(x_c; y) \sin^2 \varphi_s, \quad (2.13)$$

$$W_s(y) = W_s^* / Q_e^* = \{G(x_c; y) - F'(x_c; y)\} \cos \varphi_s \sin \varphi_s, \quad (2.14)$$

for various x_c^* / c^* . Also shown are the Falkner–Skan–Cooke (FSC) similarity profiles used in the previous investigation of Koch (1996). While there are some deviations in the first half of the plate, the FSC similarity profiles are quite accurate for $x_c^* / c^* > 0.4$.

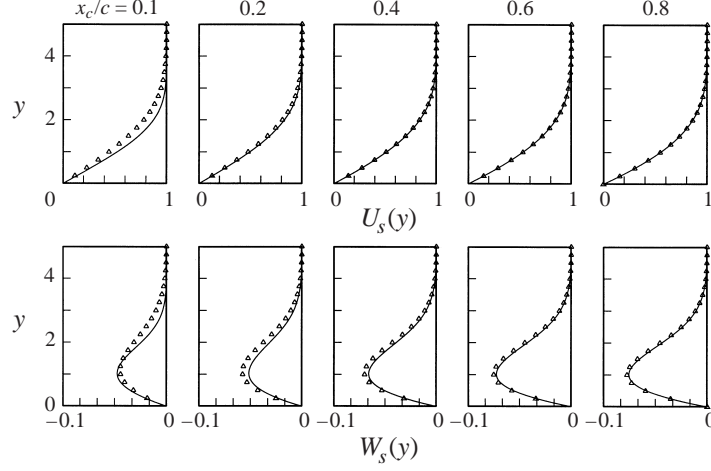


FIGURE 4. Streamwise and crossflow velocity profiles for various x_c/c . Symbols denote the Falkner–Skan–Cooke profiles, lines the non-similar boundary-layer solution.

3. Primary equilibrium solution

3.1. Governing equations

The incompressible Navier–Stokes equations are non-dimensionalized with the local reference quantities L_{ref}^* and Q_{ref}^* defined at fixed $x_c = x_{c,r}$. We are interested in oblique, travelling-wave-type equilibrium solutions which propagate in the direction $\psi_c = \arctan(\beta_c/\alpha_c)$ with the (unknown) wave speed C . Using the Galilei transformation $x'_c = x_c - C \cos \psi_c t$, $y' = y$, $z'_c = z_c - C \sin \psi_c t$, $t' = t$, and henceforth dropping the prime, the solution is steady in the moving system, i.e. $\partial/\partial t \equiv 0$. Substituting (2.1), non-dimensionalized with Q_e^* , together with (2.12) into the incompressible Navier–Stokes equations in the normal velocity (v)–normal vorticity (η) formulation, with $\eta = \partial u_c/\partial z_c - \partial w_c/\partial x_c$, we obtain for the disturbance part ($\tilde{v}, \tilde{\eta}$) in chordwise coordinates

$$\left\{ (U_c - C \cos \psi_c) \frac{\partial}{\partial x_c} + (W_c - C \sin \psi_c) \frac{\partial}{\partial z_c} \right\} \Delta_c \tilde{v} - \frac{d^2 U_c}{dy^2} \frac{\partial \tilde{v}}{\partial x_c} - \frac{d^2 W_c}{dy^2} \frac{\partial \tilde{v}}{\partial z_c} + \varepsilon_p \left\{ \frac{\partial^2 \mathcal{N}^{(2)}}{\partial x_c^2} + \frac{\partial^2 \mathcal{N}^{(2)}}{\partial z_c^2} - \frac{\partial^2 \mathcal{N}^{(1)}}{\partial x_c \partial y} - \frac{\partial^2 \mathcal{N}^{(3)}}{\partial y \partial z_c} \right\} = \frac{1}{Re} \Delta_c \Delta_c \tilde{v}, \quad (3.1)$$

$$(U_c - C \cos \psi_c) \frac{\partial \tilde{\eta}}{\partial x_c} + (W_c - C \sin \psi_c) \frac{\partial \tilde{\eta}}{\partial z_c} + \frac{dU_c}{dy} \frac{\partial \tilde{v}}{\partial z_c} - \frac{dW_c}{dy} \frac{\partial \tilde{v}}{\partial x_c} + \varepsilon_p \left\{ \frac{\partial \mathcal{N}^{(1)}}{\partial z_c} - \frac{\partial \mathcal{N}^{(3)}}{\partial x_c} \right\} = \frac{1}{Re} \Delta_c \tilde{\eta}. \quad (3.2)$$

Here Δ_c denotes the Laplacian in chordwise coordinates, and the nonlinear terms are

$$\mathcal{N}^{(1)} = \tilde{u}_c \frac{\partial \tilde{u}_c}{\partial x_c} + \tilde{v} \frac{\partial \tilde{u}_c}{\partial y} + \tilde{w}_c \frac{\partial \tilde{u}_c}{\partial z_c}, \quad (3.3a)$$

$$\mathcal{N}^{(2)} = \tilde{u}_c \frac{\partial \tilde{v}}{\partial x_c} + \tilde{v} \frac{\partial \tilde{v}}{\partial y} + \tilde{w}_c \frac{\partial \tilde{v}}{\partial z_c}, \quad (3.3b)$$

$$\mathcal{N}^{(3)} = \tilde{u}_c \frac{\partial \tilde{w}_c}{\partial x_c} + \tilde{v} \frac{\partial \tilde{w}_c}{\partial y} + \tilde{w}_c \frac{\partial \tilde{w}_c}{\partial z_c}. \quad (3.3c)$$

The velocity components \tilde{u}_c and \tilde{w}_c can be determined from the definition of normal vorticity $\tilde{\eta}$ together with the continuity equation.

Due to our parallel-flow assumption all disturbances will be periodic not only in z_c but also in x_c and can be expressed in the form of Fourier expansions

$$\left\{ \begin{array}{l} \tilde{v} \\ \tilde{\eta} \end{array} \right\} (x_c, y, z_c) = \sum_{n=-N_p}^{N_p} \left\{ \begin{array}{l} \hat{v}_n(y) \\ \hat{\eta}_n(y) \end{array} \right\} e^{i n(\alpha_c x_c + \beta_c z_c)} \quad (3.4)$$

which will be truncated at N_p . The modal functions $\hat{v}_n(y)$ and $\hat{\eta}_n(y)$ are complex but reality of the physical solution implies

$$\hat{v}_{-n} = \hat{v}_n^\dagger, \quad \hat{\eta}_{-n} = \hat{\eta}_n^\dagger,$$

such that only modes with $n \geq 0$ need to be considered. The dagger denotes the complex conjugate. Substituting (3.4) into equations (3.1) and (3.2) and balancing exponential terms, we obtain the *modal equations* for $0 < n \leq N_p$

$$\left\{ \frac{1}{Re} \left(\frac{d^2}{dy^2} - n^2 k^2 \right)^2 - ink \left[(U_\psi - C) \left(\frac{d^2}{dy^2} - n^2 k^2 \right) - \frac{d^2 U_\psi}{dy^2} \right] \right\} \hat{v}_n = \varepsilon_p \sum_{r=-N_p}^{N_p} \mathcal{N}_{n-r,r}^{OS}, \quad (3.5)$$

$$\left\{ \frac{1}{Re} \left(\frac{d^2}{dy^2} - n^2 k^2 \right) - ink(U_\psi - C) \right\} \hat{\eta}_n + ink \frac{dW_\psi}{dy} \hat{v}_n = \varepsilon_p \sum_{r=-N_p}^{N_p} \mathcal{N}_{n-r,r}^{SQ}, \quad (3.6)$$

subject to the homogeneous boundary conditions

$$\begin{aligned} \hat{v}_n(y) = d\hat{v}_n(y)/dy = \hat{\eta}_n(y) = 0, \quad y = 0, \\ \hat{v}_n(y) = d\hat{v}_n(y)/dy = \hat{\eta}_n(y) = 0, \quad y \rightarrow \infty. \end{aligned}$$

Here $k = (\alpha_c^2 + \beta_c^2)^{1/2}$ is the magnitude of the wavenumber vector in the wave-oriented coordinate system (x_ψ, y, z_ψ) , where x_ψ is in the direction of the wavenumber vector making the angle $\psi_c = \arctan(\beta_c/\alpha_c)$ with the x_c -direction, cf. figure 2. The corresponding base flow components are (*Stuart transformation*)

$$U_\psi(y) = U_c(y) \cos \psi_c + W_c(y) \sin \psi_c, \quad (3.7)$$

$$W_\psi(y) = -U_c(y) \sin \psi_c + W_c(y) \cos \psi_c. \quad (3.8)$$

Using the definition of the vorticity vector (ξ, η, ζ) together with the continuity equation we obtain

$$\begin{aligned} \hat{u}_n &= i(\alpha_c d\hat{v}_n/dy - \beta_c \hat{\eta}_n)/(nk^2), \\ \hat{w}_n &= i(\beta_c d\hat{v}_n/dy + \alpha_c \hat{\eta}_n)/(nk^2), \\ \hat{\xi}_n &= i(\alpha_c d\hat{\eta}_n/dy + \beta_c d^2 \hat{v}_n/dy^2)/(nk^2) - in\beta_c \hat{v}_n, \\ \hat{\zeta}_n &= i(\beta_c d\hat{\eta}_n/dy - \alpha_c d^2 \hat{v}_n/dy^2)/(nk^2) + in\alpha_c \hat{v}_n. \end{aligned}$$

With these expressions the nonlinear convolution terms in equations (3.5), (3.6) can be written in terms of $(\hat{v}, \hat{\eta})$:

$$\begin{aligned} \mathcal{N}_{v,r}^{OS} &= \frac{r+v}{v} \left\{ \hat{v}_v \left(\frac{d^2}{dy^2} - r^2 k^2 \right) \frac{d\hat{v}_r}{dy} - \frac{d\hat{v}_v}{dy} \left(\frac{d^2}{dy^2} - r^2 k^2 \right) \hat{v}_r \right\}, \\ \mathcal{N}_{v,r}^{SQ} &= \frac{r}{v} \left(\hat{v}_r \frac{d\hat{\eta}_v}{dy} - \hat{\eta}_r \frac{d\hat{v}_v}{dy} \right) + \hat{v}_v \frac{d\hat{\eta}_r}{dy} - \hat{\eta}_v \frac{d\hat{v}_r}{dy}. \end{aligned}$$

The mean flow distortion components \hat{u}_0 and \hat{w}_0 require a separate treatment of those convolution terms containing them, i.e.

$$\sum_{r=-N_p}^{N_p} \mathcal{N}_{n-r,r} = \mathcal{N}_{n,0} + \mathcal{N}_{0,n} + \sum_{r=-N_p}^{N_p}{}'' \mathcal{N}_{n-r,r},$$

where \sum'' denotes the sum over the remaining terms. In particular we find

$$\begin{aligned} \mathcal{N}_{n,0}^{OS} + \mathcal{N}_{0,n}^{OS} &= in\alpha_c \{ \hat{u}_0 (d^2 \hat{v}_n / dy^2 - n^2 k^2 \hat{v}_n) - \hat{v}_n d^2 \hat{u}_0 / dy^2 \} \\ &\quad + in\beta_c \{ \hat{w}_0 (d^2 \hat{v}_n / dy^2 - n^2 k^2 \hat{v}_n) - \hat{v}_n d^2 \hat{w}_0 / dy^2 \}, \\ \mathcal{N}_{n,0}^{SQ} + \mathcal{N}_{0,n}^{SQ} &= in\alpha_c \{ \hat{u}_0 \hat{\eta}_n - \hat{v}_n d \hat{w}_0 / dy \} + in\beta_c \{ \hat{w}_0 \hat{\eta}_n + \hat{v}_n d \hat{u}_0 / dy \}. \end{aligned}$$

3.2. Mean flow distortion

As discussed by Milinazzo & Saffman (1985) for Blasius boundary-layer flow, the assumption of chordwise periodicity constitutes a fundamental difficulty for the local theory. In order to formulate at least a mathematically well-posed problem they introduced a *fictitious force term* into the Navier–Stokes equations which renders the locally parallel boundary-layer base flow an exact solution of the modified equations. With various modifications this *ad hoc* procedure has been used extensively for boundary-layer flows in temporal DNS, cf. the original work of Wray & Hussaini (1984) or the review by Kleiser & Zang (1991), and local bifurcation analyses, cf. Milinazzo & Saffman (1985) or Koch (1992). While one can argue about the physical relevance of the non-rational force-term formulation, the results seemed to give at least qualitatively correct results for two-dimensional boundary layers.

Using a FSC model flow with $\beta_H = 0.6$ and $\varphi_s = 45^\circ$ Meyer & Kleiser (1988) used the force-term formulation to compute quasi-two-dimensional temporal equilibria for stationary crossflow vortices with $k = 0.3557$ and $\psi_s = (\psi_c - \varphi_s) = 85.6^\circ$. They found steady equilibria below $Re \approx 220$ and time-periodic equilibria above, with a supercritical Hopf bifurcation near $Re \approx 220$. For the same problem and $Re = 220$ Fischer (1995) performed a weakly nonlinear analysis using the parallel-flow assumption and achieved good agreement with the results of Meyer & Kleiser (1988). At this low Reynolds number the mean-flow disturbance profiles of figure 5 in Fischer (1995) could be reproduced almost exactly by extending the numerical force-term bifurcation analysis of Koch (1992). However, in an attempt to approximate the experimentally observed saturation states in the second half of the plate, where the Reynolds numbers and amplitudes are larger, a physically abnormal overshoot of the streamwise mean flow velocity was obtained. To our knowledge the only other paper where a similar observation has been reported is the long-time temporal simulation of Corral & Jiménez (1992), cf. their figure 8. They speculate that the force term does not represent the flow correctly over such long time scales and therefore is the reason for this overshoot.

This brings us back to the unphysical parallel-flow assumption. As shown by Herbert (1974) and elaborated by Bertolotti (1991), the convective and viscous terms are of equal order for wavenumbers approaching zero. Hence, for large Re the parabolic boundary-layer equations govern not only the laminar base flow but also the mean flow distortion ($\varepsilon_p \hat{u}_0(y)$, $\varepsilon_p \hat{v}_0(y)$, $\varepsilon_p \hat{w}_0(y)$). In an attempt to approximate the solution locally by an ordinary differential equation Herbert (1974) and Bertolotti (1991) assumed the whole mean flow to be locally self-similar. In the following we shall also use this locally self-similar approach. However, we have to stress the fact

that this is only an approximation because the nonlinear forcing terms are by no means self-similar. We shall test the validity of this self-similarity approximation by comparing the results with PSE and spatial DNS computations.

Following Herbert (1974) we therefore combine the mean flow distortion with the laminar base flow and apply the boundary-layer scaling to the total mean flow

$$(U_{m,c}, V_{m,c}, W_{m,c}) = (U_c(x_c, \chi) + \varepsilon_p \hat{u}_0(x_c, \chi), \varepsilon_p \hat{v}_0(x_c, \chi), W_c(x_c, \chi) + \varepsilon_p \hat{w}_0(x_c, \chi)). \quad (3.9)$$

Here χ denotes the similarity variable introduced by (2.5). Due to the infinite-swept-wing assumption the total mean flow is independent of z_c and the continuity equation defines a mean flow stream function $\Psi_{m,c}(x_c, \chi)$ such that

$$U_{m,c}(x_c, \chi) = \partial \Psi_{m,c} / \partial \chi, \quad V_{m,c}(x_c, \chi) = -\partial \Psi_{m,c} / \partial x_c.$$

Balancing exponential terms we obtain the *mean flow equations* valid for large Re :

$$\frac{1}{Re} \frac{\partial^3 \Psi_{m,c}}{\partial \chi^3} - \frac{\partial \Psi_{m,c}}{\partial \chi} \frac{\partial^2 \Psi_{m,c}}{\partial x_c \partial \chi} + \frac{\partial \Psi_{m,c}}{\partial x_c} \frac{\partial^2 \Psi_{m,c}}{\partial \chi^2} + U_{c,e} \frac{dU_{c,e}}{dx_c} = \varepsilon_p^2 \sum_{r=1}^{N_p} \mathcal{N}_{-r,r}^{(1)}, \quad (3.10)$$

$$\frac{1}{Re} \frac{\partial^2 W_{m,c}}{\partial \chi^2} - \frac{\partial \Psi_{m,c}}{\partial \chi} \frac{\partial W_{m,c}}{\partial x_c} + \frac{\partial \Psi_{m,c}}{\partial x_c} \frac{\partial W_{m,c}}{\partial \chi} = \varepsilon_p^2 \sum_{r=1}^{N_p} \mathcal{N}_{-r,r}^{(3)}, \quad (3.11)$$

subject to the boundary conditions

$$\begin{aligned} \Psi_{m,c}(x_c, \chi) &= \partial \Psi_{m,c}(x_c, \chi) / \partial \chi = W_{m,c}(x_c, \chi) = 0, \chi = 0, \\ \partial \Psi_{m,c}(x_c, \chi) / \partial \chi &= \cos \varphi_s, \quad W_{m,c}(x_c, \chi) = \sin \varphi_s, \chi \rightarrow \infty. \end{aligned}$$

Here the nonlinear terms (3.3a) and (3.3c) can again be rewritten in terms of $(\hat{v}, \hat{\eta})$

$$\begin{aligned} \mathcal{N}_{-r,r}^{(1)} &= -\frac{2}{rk^2} \operatorname{Im} \left\{ \alpha_c \frac{d^2 \hat{v}_r}{d\chi^2} \hat{v}_r^\dagger - \beta_c \frac{d}{d\chi} (\hat{\eta}_r \hat{v}_r^\dagger) \right\}, \\ \mathcal{N}_{-r,r}^{(3)} &= -\frac{2}{rk^2} \operatorname{Im} \left\{ \beta_c \frac{d^2 \hat{v}_r}{d\chi^2} \hat{v}_r^\dagger + \alpha_c \frac{d}{d\chi} (\hat{\eta}_r \hat{v}_r^\dagger) \right\}, \end{aligned}$$

with Im denoting the imaginary part.

In equations (3.10) and (3.11) the dilemma with the parallel-flow assumption becomes apparent because they contain derivatives in x_c -direction. Following the suggestion of Herbert (1974) we use the local similarity assumption for the mean flow distortion

$$\Psi_{m,c}(x_c, y) = \left(\frac{U_{c,e}^*(x_{c,r}^*) x_{c,r}^*}{U_{c,e}^*(x_{c,r}^*) x_{c,r}^*} \right)^{1/2} \{F(x_c, \chi) + \varepsilon_p f_0(\chi)\} \cos \varphi_s(x_{c,r}^*), \quad (3.12)$$

$$W_{m,c}(x_c, y) = \{G(x_c, \chi) + \varepsilon_p g_0(\chi)\} \sin \varphi_s(x_{c,r}^*) \quad (3.13)$$

to approximate the chordwise variation of the total mean flow. Here $F(x_c, \chi)$ and $G(x_c, \chi)$ denote the non-similar laminar base flow solution of §2.2. Substituting (3.12) and (3.13) into equations (3.10), (3.11), subtracting out the laminar base flow and observing that

$$x_{c,r} = (U_{c,e}^*(x_{c,r}^*) x_{c,r}^* / v^*)^{1/2} = Re \cos \varphi_s(x_{c,r}^*),$$

we obtain approximate *mean flow distortion equations* by letting $x_c \rightarrow x_{c,r}$ such that $\chi \rightarrow y$

$$\frac{\cos \varphi_s(x_{c,r}^*)}{Re} \left\{ f_0''' + \frac{1}{2 - \beta_H} (F'' f_0 + F f_0'' + \varepsilon_p f_0 f_0'') - \frac{\beta_H}{2 - \beta_H} (2F' f_0' + \varepsilon_p f_0'^2) \right. \\ \left. + \cos \varphi_s(x_{c,r}^*) Re \left(\frac{\partial F}{\partial x_c} f_0'' - \frac{\partial F'}{\partial x_c} f_0' \right) \right\} = \varepsilon_p \sum_{r=1}^{N_p} \mathcal{N}_{-r,r}^{(1)}, \quad (3.14)$$

$$\frac{\sin \varphi_s(x_{c,r}^*)}{Re} \left\{ g_0'' + \frac{1}{2 - \beta_H} (G' f_0 + F g_0' + \varepsilon_p f_0 g_0') \right. \\ \left. + \cos \varphi_s(x_{c,r}^*) Re \left(\frac{\partial F}{\partial x_c} g_0' - \frac{\partial G}{\partial x_c} f_0' \right) \right\} = \varepsilon_p \sum_{r=1}^{N_p} \mathcal{N}_{-r,r}^{(3)}, \quad (3.15)$$

with the homogeneous boundary conditions

$$f_0(y) = f_0'(y) = g_0(y) = 0, \quad y = 0, \\ f_0'(y) = g_0(y) = 0, \quad y \rightarrow \infty.$$

From (3.12), (3.13) we find for $x_c \rightarrow x_{c,r}$

$$\hat{u}_0(y) = f_0'(y) \cos \varphi_s(x_{c,r}^*), \quad \hat{w}_0(y) = g_0(y) \sin \varphi_s(x_{c,r}^*). \quad (3.16)$$

3.3. Numerical solution procedure

For the numerical solution the governing modal equations (3.5), (3.6) and the mean flow distortion equations (3.14), (3.15) are converted into algebraic form by means of Chebyshev collocation, with due consideration of the corresponding boundary conditions. For this purpose the semi-infinite domain $y \in [0, \infty)$ is mapped into the finite domain $\chi \in [1, 0)$ via the exponential transformation

$$\chi = \exp(-y/y_0), \quad y = -y_0 \ln \chi. \quad (3.17)$$

In general we choose $y_0 = 15$ and truncate the Fourier expansion (3.4) at $N_p = 4$. In the wall-normal direction we use $K = 55$ collocation points for all results presented unless otherwise noted. The low-resolution truncation at $N_p = 4$ as well as the v - η formulation instead of the primitive variables formulation are means of limiting the size of the Jacobian in the Newton-Raphson iteration of our continuation method. To take advantage of symmetry properties it is assumed that the laminar mean flow at the K collocation points

$$\chi_j = \cos [j\pi/(2K - 1)], \quad j = 0, \dots, K - 1, \quad (3.18)$$

can be continued symmetrically into $-1 \leq \chi < 0$. Spurious unstable modes are avoided by employing Ehrenstein's method for the implementation of the boundary conditions, essentially a reduction to a system of at most second-order differential equations, cf. the appendix in Brevdo (1992b). Derivatives are computed by the collocation matrix method, cf. Canuto *et al.* (1987). To fix the amplitude ε_p and phase of the solution we add the *local normalization condition*

$$\hat{v}_1(y_{norm}) = 1, \quad (3.19)$$

where we take y_{norm} as the tenth collocation point. The choice of y_{norm} is arbitrary, but \hat{v}_1 must not be too close to zero at y_{norm} .

If we introduce the definitions

$$f_{0j} = f_0(y_j); \quad g_{0j} = g_0(y_j); \quad \hat{v}_{nj} = \hat{v}_n(y_j); \quad \hat{\eta}_{nj} = \hat{\eta}_n(y_j), \\ 1 \leq n \leq N_p, \quad 0 \leq j \leq K - 1,$$

Chebyshev collocation transforms our governing equations (3.5), (3.6), (3.14) and (3.15) together with the normalizing condition (3.19) into a system of $2(1 + 2N_p)(K - 1) + 2$ nonlinear (real) algebraic equations of the form

$$\mathbf{F}(\mathbf{y}; \mathbf{A}) = 0. \tag{3.20}$$

The (real) solution vector

$$\mathbf{y} = \{f_{0j}, g_{0j}; \text{Re}(\hat{v}_{nj}), \text{Im}(\hat{v}_{nj}), \text{Re}(\hat{\eta}_{nj}), \text{Im}(\hat{\eta}_{nj}); C, \varepsilon_p\}, \\ 1 \leq n \leq N_p, \quad 1 \leq j \leq K - 1,$$

contains the $2(1 + 2N_p)(K - 1)$ unknown modal values at the $K - 1$ interior collocation points together with the unknown wave speed C and amplitude ε_p . Here $\text{Re}(z)$ and $\text{Im}(z)$ denote the real and imaginary part of z . The parameter vector \mathbf{A} contains the parameters controlling the solution. In general we are interested in finding the solution of (3.20) as a single parameter, the so-called *bifurcation parameter* λ , is varied while all other parameters are kept fixed, for example $\lambda = \alpha_c$ out of $\mathbf{A} = (\alpha_c, \beta_c, Re)$. For this branch tracing or path following procedure we use the *continuation method*, cf. Keller (1977) or the monograph by Seydel (1994). To avoid the singularity of ordinary continuation in λ at a turning point (simple fold point) where the Jacobian \mathbf{F}_y vanishes, an additional parameterizing equation $P(\mathbf{y}, \lambda, s) = 0$ is added to formulate the extended system

$$\mathbf{G}(\mathbf{Y}; s) \equiv \begin{pmatrix} \mathbf{F}(\mathbf{Y}) \\ P(\mathbf{Y}; s) \end{pmatrix} = 0; \quad \mathbf{Y} = \begin{pmatrix} \mathbf{y} \\ \lambda \end{pmatrix}. \tag{3.21}$$

Here s denotes an arclength parameter. Usually the *pseudo-arclength* parameterization of Keller (1977)

$$P(\mathbf{y}, \lambda, s) \equiv \theta \sum_i \{y_i(s) - y_i(s_0)\} (dy_i/ds)(s_0) \\ + (1 - \theta) \{\lambda(s) - \lambda(s_0)\} (d\lambda/ds)(s_0) - (s - s_0) = 0$$

is used, where s_0 denotes the pseudo-arclength parameter at the previously computed point. The detuning parameter $0 < \theta < 1$ allows us to place different emphasis on \mathbf{y} or λ and the sum is to be extended over all $2(1 + 2N_p)(K - 1) + 2$ components of the solution vector \mathbf{y} .

Starting with a known solution $\mathbf{Y}(s_0)$ at $s = s_0$, which in our case is either a solution on the linear neutral surface or a previously computed nonlinear solution, an initial approximation $\mathbf{Y}^{(0)}(s)$ of the new solution at s can be obtained by means of the simple tangent predictor

$$\mathbf{Y}^{(0)}(s) = \mathbf{Y}(s_0) + (s - s_0) (d\mathbf{Y}/ds)(s_0),$$

where $(d\mathbf{Y}/ds)(s_0)$ is already available from the Newton–Raphson iteration at the previous step. The approximate solution $\mathbf{Y}^{(0)}(s)$ is then corrected by Newton–Raphson iteration of the extended system (3.21), which converges rapidly for a suitably chosen step size $(s - s_0)$.

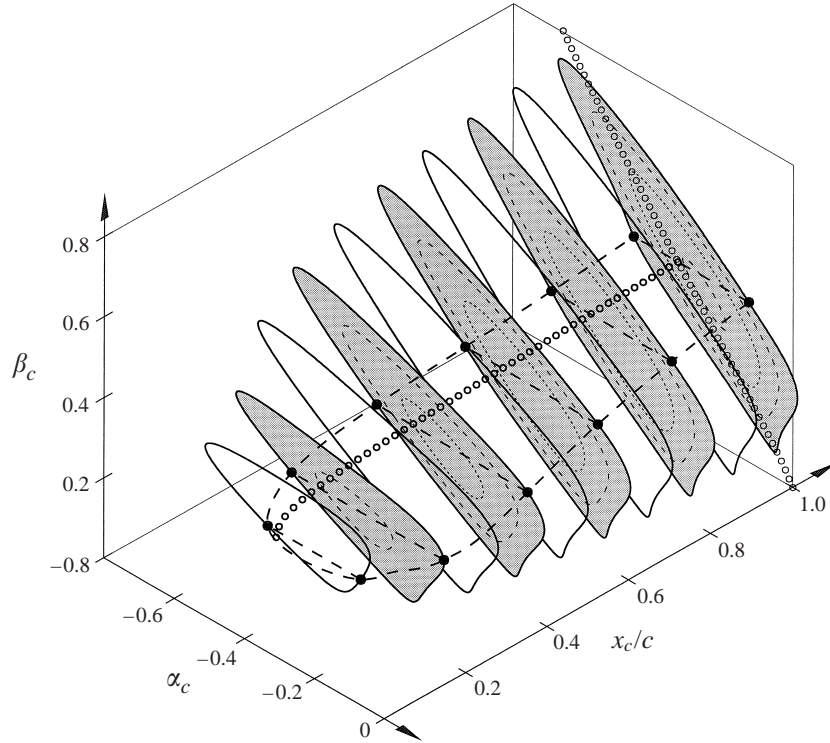


FIGURE 5. Cuts through linear neutral surface $\text{Im}\{\omega(\alpha_c, \beta_c, x_c/c)\} = 0$ at $x_c/c = 0.1, 0.2, \dots, 1.0$ for $Q_\infty^* = 19 \text{ m s}^{-1}$, $\varphi_\infty = 42.5^\circ$ and $K = 45$.

3.4. Linear and nonlinear neutral surface

As noted in §3.3 the linear neutral surface is the starting point for our continuation procedure and therefore has to be computed first. With $n = 1$, $\varepsilon_p = 0$ and $\omega = kC$ equations (3.5), (3.6) reduce to the temporal primary stability equations for the (complex) frequency ω . Figure 5 shows the results in the form of various cuts through the linear neutral surface $\text{Im}(\omega) = 0$ for our quasi-parallel swept-plate flow with $Q_\infty = 19 \text{ m s}^{-1}$ and $\varphi_\infty = 42.5^\circ$. Temporal amplification curves for $\text{Im}(\omega) = 0.0025$, 0.005 and 0.0075 are shown as thin dashed curves in every second (shaded) $x_c/c = \text{const}$ cut. In the $x_c/c = 1$ cut the zero-frequency line $\text{Re}(\omega) = 0$ is marked by small circles.

From this linear neutral surface the solution can now be continued into the nonlinear regime $\varepsilon_p > 0$. Instead of the amplitude ε_p it is customary to use the *total fluctuation energy* E per unit mass, non-dimensionalized with $U_{ref}^* L_{ref}^*$, as a measure of nonlinearity, i.e.

$$E = 2 \sum_{n=1}^{N_p} E_n, \quad E_n = \varepsilon_p^2 \int_0^\infty \{|\hat{u}_n(y)|^2 + |\hat{v}_n(y)|^2 + |\hat{w}_n(y)|^2\} dy.$$

The factor 2 takes care of the modes from $n = -1$ to $n = -N_p$. The linear neutral surface depends on the three parameters α_c, β_c and x_c/c (or equivalently Re). Nonlinearity adds the fourth parameter E (or equivalently ε_p). Due to the infinite-swept-wing assumption the dimensional spanwise disturbance wavelength $\lambda_{z_c}^*$ remains constant as

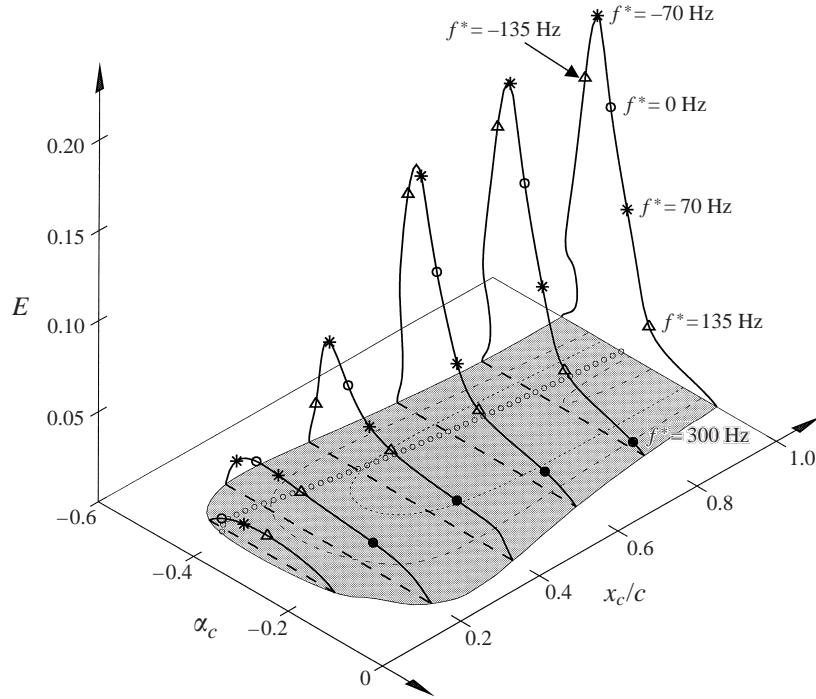


FIGURE 6. Nonlinear neutral surface $E(\alpha_c, x_c/c)$ for constant spanwise wavelength $\lambda_{z_c}^* = 12$ mm. $Q_\infty^* = 19 \text{ m s}^{-1}$, $\varphi_\infty = 42.5^\circ$ with $N_p = 4$.

a single wave travels downstream. In order to limit our parameter variation we selected that particular cut through the linear neutral surface which keeps $\lambda_{z_c}^* = 12$ mm constant. This is close to the experimentally observed value for stationary crossflow vortices, cf. Müller (1995). $\lambda_{z_c}^* = 12$ mm is also close to the critical spanwise wavelength for stationary crossflow vortices. In figure 5 the (parallel-flow) neutral curve for $\beta_c = \beta_c^* L_{ref}^* = 2\pi L_{ref}^* / \lambda_{z_c}^*$ corresponding to $\lambda_{z_c}^* = 12$ mm is shown by the thick dashed curve. Notice that due to the local reference length L_{ref}^* varying with x_c/c the value of β_c also varies with x_c/c . The zero-frequency line $\text{Re}(\omega) = 0$ in the $\lambda_{z_c}^* = 12$ mm cut is again marked by small circles. We see that travelling crossflow vortices with $\lambda_{z_c}^* = 12$ mm become unstable slightly closer to the leading edge $x_c/c = 0$ than stationary crossflow vortices. These correspond to the experimentally observed low-frequency waves travelling towards the leading edge.

The bounding curve of this particular $\lambda_{z_c}^* = 12$ mm cut through the linear neutral surface, reshown in figure 6 as the boundary of the shaded area, is the starting point for our nonlinear continuation procedure. The thin dashed curves for $E = 0$ mark again the temporal amplification curves $\text{Im}(\omega) = 0.0025, 0.005$ and 0.0075 and give an idea about the linear growth under the parallel flow assumption. The line formed by the small open circles represents the zero-frequency line $\text{Re}(\omega) = 0$ for the linear problem with $\lambda_{z_c}^* = 12$ mm. Fixing x_c/c (i.e. Re) together with $\lambda_{z_c}^*$ (i.e. β_c) we vary α_c in our continuation procedure and obtain the nonlinear equilibria for $N_p = 4$ shown as solid curves in figure 6. The low resolution $N_p = 4$ has been chosen as a compromise between necessary computation time and accuracy. For the simpler approximation using FSC base flow profiles preliminary results were published in Koch (1996). On the equilibrium curves the large open circles depict the zero-frequency results for

x_c^*/c^*	β_H	φ_s (deg.)	Q_{ref}^* (m s ⁻¹)	L_{ref}^* (mm)	Re
0.1	0.4549	67.5397	13.8898	0.3772	346.9673
0.2	0.5408	62.4763	14.4744	0.4751	455.4462
0.3	0.5771	58.6143	15.0363	0.5378	535.5424
0.4	0.5972	55.4872	15.5779	0.5849	603.4576
0.5	0.6099	52.8648	16.1014	0.6232	664.5121
0.6	0.6187	50.6132	16.6083	0.6556	721.1089
0.7	0.6251	48.6464	17.1002	0.6839	774.5382
0.8	0.6300	46.9055	17.5784	0.7092	825.5734
0.9	0.6339	45.3482	18.0438	0.7320	874.7164
1.0	0.6370	43.9427	18.4976	0.7529	922.3121

TABLE 1. Local reference quantities

stationary crossflow vortices. The other symbols mark travelling crossflow vortices with various (dimensional) frequencies

$$f^* [\text{Hz}] = \frac{Ck Q_{ref}^*}{2\pi L_{ref}^*},$$

ranging from 0 to 300 Hz, where C is the computed nonlinear wave speed of the equilibrium solution and $k = (\alpha_c^2 + \beta_c^2)^{1/2}$. Positive frequencies designate crossflow vortices propagating towards the leading edge, negative frequencies specify crossflow vortices travelling away from the leading edge. As can be seen from figure 6 the latter travelling waves become neutral farther away from the leading edge than the stationary crossflow vortices and their importance for transition is not yet clear. We also notice that the nonlinear equilibrium energy of waves with phase velocities oriented towards the leading edge is considerably lower than the energy of the stationary vortex. This trend is in line with experimental and DNS observations that the saturation amplitude of travelling waves is lower than that of the stationary vortex.

However, the question of utmost interest is how well do these local temporal equilibrium solutions approximate actual spatial simulations. For this purpose we performed a nonlinear PSE analysis, cf. Bertolotti, Herbert & Spalart (1992) or Herbert (1997), for the stationary vortex $f^* = 0$ using the multi-domain spectral code with the same low resolution $N_p = 4$ and widely varying initial amplitudes. In spatial simulations more relevant global reference quantities are usually used which allow a direct comparison between different chordwise stations. To facilitate a comparison with global reference quantities we include a list of our local reference quantities in table 1 which was computed with $v^* = 0.151 \times 10^{-4} \text{ m}^2 \text{ s}^{-1}$. Our PSE analysis uses the same non-self-similar boundary-layer base flow (cf. figure 4) as our equilibrium solution. The results of this comparison are shown in figure 7 on the commonly used semi-log scale as well as on a linear scale. The semi-log scale clearly shows the widely varying initial conditions for the fundamental mode imposed upstream from the neutral point (marked by an arrow) such that the PSE results decay first before becoming amplified. To get a feeling for the initial conditions which are relevant for the DLR swept-plate experiment we also included the stationary vortex results of Bertolotti (1996) (marked by the dotted curve with the star symbols) for a row of steady surface bumps at $x_c/c = 0.08$ although these results are for slightly different free-stream conditions. In Bertolotti (1996) it has been demonstrated that for a true

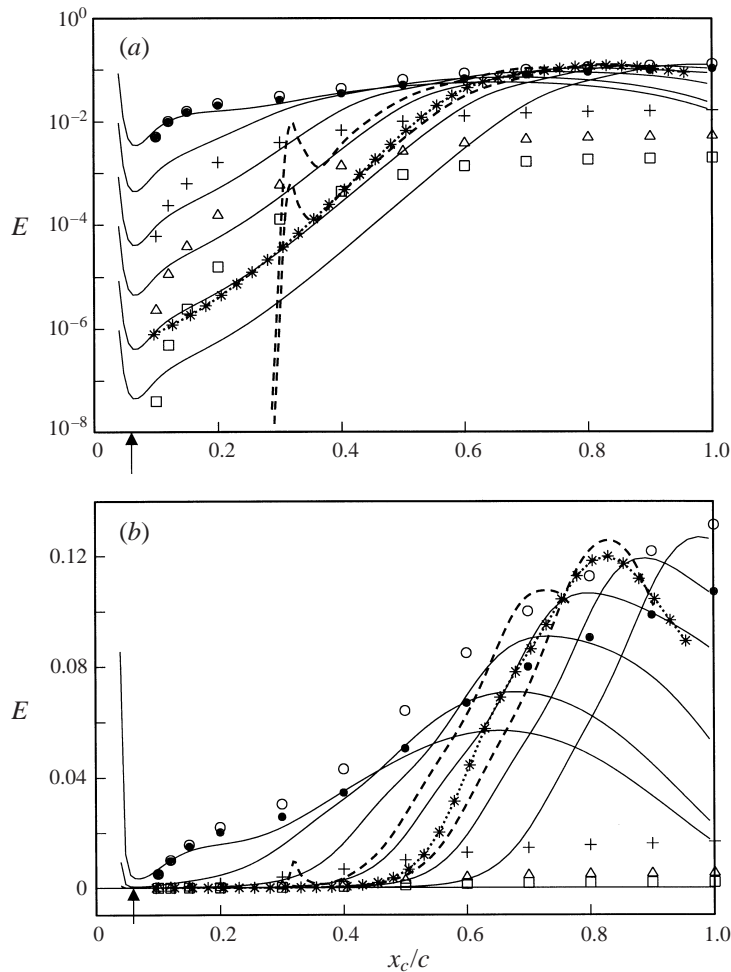


FIGURE 7. Total fluctuation energy E of steady crossflow vortices as a function of chordwise distance x_c/c for $\lambda_{z_c}^* = 12$ mm, $Q_\infty^* = 19$ m s $^{-1}$ and $\varphi_\infty = 42.5^\circ$: (a) semi-log scale, (b) linear scale. The various solid curves depict our PSE results for widely varying initial conditions. The two dashed curves are unpublished spatial DNS results of Kloker & Bonfigli (1998) for two differing initial conditions. The symbols mark our local zero-frequency equilibrium results with $N_p = 4$: open circles give the total fluctuation energy E , the other symbols indicate the contributions of the four modal energies E_n namely $n = 1$ (solid circle), $n = 2$ (cross), $n = 3$ (triangle) and $n = 4$ (open square). The arrow marks the neutral point and the dotted curve with the starred symbols shows the stationary vortex result of Bertolotti (1996) initiated by a row of steady surface bumps at $x_c/c = 0.08$.

comparison with the experiment one has to include travelling modes as well. In wind tunnel experiments these travelling modes are always excited by the free-stream turbulence contrary to the low-turbulence environment of free flight.

The linear scale can be used to demonstrate the saturation behaviour in more detail. Also depicted are the modal energies of the first four Fourier modes of the equilibrium solution, demonstrating that the rather low resolution $N_p = 4$ is accurate enough for the total fluctuation energy E . The various PSE results seem to approach the equilibrium result but then decay again. A similar oscillatory behaviour had been observed by Malik *et al.* (1994) and a check with the completely independent compact finite difference PSE code NOLOT (for a description of the linear version of the code

see Hein *et al.* (1994)) produced practically identical results. While we had anticipated deviations due to our simplifying assumptions in obtaining the equilibrium solution, we expected all PSE results to coalesce into a single unique ‘saturation’ curve. Using an improved version of the spatial DNS code of Müller (1995), M. Kloker & G. Bonfigli (1998 personal communication; see also Bonfigli & Kloker 1999) recently recomputed the spatial evolution of stationary crossflow vortices in the DLR swept-plate experiment for varying initial conditions and observed similar effects. Two of their unpublished results are included in figure 7 as dashed curves and compare very well with the PSE results (the differences are probably due to a slightly different base flow and a different implementation of the initial disturbance).

The unexpected behaviour that for high initial amplitudes of the stationary crossflow vortices the ‘saturation’ maxima are lower and further upstream than for low initial amplitudes indicates a spatial bifurcation analogous to the one observed by Meyer & Kleiser (1988) in their temporal DNS results. We are also grateful to a referee for pointing out that this spatially oscillating behaviour has been observed not only in PSE computations, cf. Malik *et al.* (1994), but also in solutions obtained by nonlinear critical layer theory, see Smith *et al.* (1993), Gajjar (1996) or Brown & Smith (1996). Using temporal DNS (and the force-term formulation) for a FSC base flow with $\beta_H = 0.6$ and $\varphi_s = 45^\circ$ Meyer (1989) found stationary equilibria independent of the initial amplitude for the low Reynolds number $Re = 260$. Wagner (1992) extended the temporal results of Meyer (1989) and computed time-periodic equilibria for the higher Reynolds number $Re = 826$ using very similar values of β_H and φ_s . The conclusion was that under the assumption of quasi-two-dimensionality the stationary equilibrium solution undergoes a Hopf bifurcation near $Re = 300$ ending up with a stable finite-amplitude travelling wave. These findings were in agreement with temporal stability computations of equilibrium solutions obtained by applying the force-term formulation (compare Koch 1992; Fischer 1995). In analogy to this temporal behaviour we arrive at the following conclusion: our equilibrium solution must become spatially unstable with respect to streamwise disturbances at some x_c/c and the slowly varying PSE solutions in figure 7 are the spatially oscillating stable solutions after bifurcation.

A spatial secondary stability analysis could prove this directly. However, we had already reached the storage limits of our workstation with the temporal analysis of §4, and therefore used the following procedure to demonstrate the spatial bifurcation. The bifurcation point, $x_{c,bif}$, divides the chord direction into an upstream region $x_c < x_{c,bif}$ and a downstream region $x_c > x_{c,bif}$. The bifurcation is of the Hopf type, leading to solutions steady in time but oscillatory in space when $x_c > x_{c,bif}$. The oscillatory motion in space is mixed with, and obscured by, the spatial development of the boundary layer. However, in a spatial, nonlinear, PSE computation the two effects can be separated artificially by freezing the laminar, undisturbed boundary layer flow past a location $x_{c,fix}$, together with the local Reynolds number, and continuing the computation in x_c . Due to the freezing, the coordinate $x_{c,pseudo} = x_c$ for $x_c > x_{c,fix}$ becomes a pseudo-coordinate. Evidence of a spatial bifurcation appears then as a periodic oscillation in $x_{c,pseudo}$ of the nonlinear solution when the freezing point is downstream of the bifurcation point $x_{c,fix} > x_{c,bif}$, and as a steady solution in $x_{c,pseudo}$ when $x_{c,fix} < x_{c,bif}$.

Figure 8 synthesizes the results of several computations into one figure. The freezing point used in each of the computations is shown along the axis labelled $x_{c,fix}/c$. The steady or oscillatory solutions develop along increasing $x_{c,pseudo}/c$. Freezing the laminar mean flow at $x_{c,fix}/c = 0.1$ results in a solution that increases rapidly

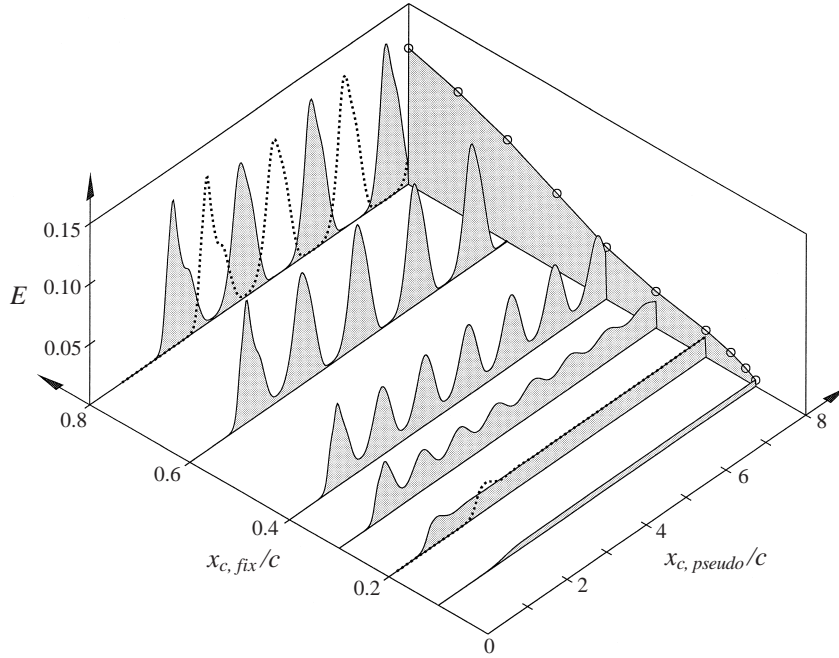


FIGURE 8. Steady crossflow vortices for $\lambda_{z_c}^* = 12$ mm, $Q_\infty^* = 19$ m s $^{-1}$ and $\varphi_\infty = 42.5^\circ$: PSE results for a boundary-layer base flow frozen at various $x_{c,fix}/c$. The curve with circles at $x_{c,pseudo}/c = 8.0$ marks the equilibrium solution result of figure 7.

in energy at about $x_{c,pseudo}/c = 1.5$ and saturates at a constant value, indicating that the bifurcation point occurs at higher chord coordinates. The same behaviour happens for $x_{c,fix}/c = 0.2$, although now a transient overshoot appears before the solution reaches the final stationary state. Different initial amplitudes for the steady crossflow vortices change only the transient behaviour, as indicated by the dotted line for the case $x_{c,fix}/c = 0.2$. Freezing the laminar base flow at $x_{c,fix}/c > 0.3$ yields solutions that oscillate indefinitely with increasing $x_{c,pseudo}$, with a wavelength of the order of the chord length of the swept plate. Unfortunately, this large wavelength hinders experimental verification, since the laminar mean flow cannot be frozen in a laboratory. Different initial amplitudes result in a phase shift of the periodic solution but not in a change of the amplitude of the oscillation, as indicated by the dotted curve in the result for $x_{c,fix}/c = 0.8$. The vertical plane positioned at $x_{c,pseudo}/c = 8.0$ in figure 8 allows one to compare the amplitude of both the steady and the oscillatory solutions with the amplitude of the equilibrium solution. The circles on this vertical plane correspond to the circles in figure 7.

The bifurcation explains why there is no ‘unique’ saturation curve for our PSE results in figure 7: after a spatial bifurcation near $x_c/c = 0.3$ only the spatially oscillating solution is stable with respect to steady streamwise disturbances. Naturally, for the non-parallel boundary layer the solution is only approximately periodic. It is a mere coincidence that the equilibrium solution appears to be the envelope of the slowly varying spatial PSE solutions for different initial amplitudes, because after bifurcation the two solutions represent different solution branches. The small discrepancies in figure 8 between the saturated PSE solutions and the equilibrium solution *before* bifurcation must be due to the similarity approximation in our local

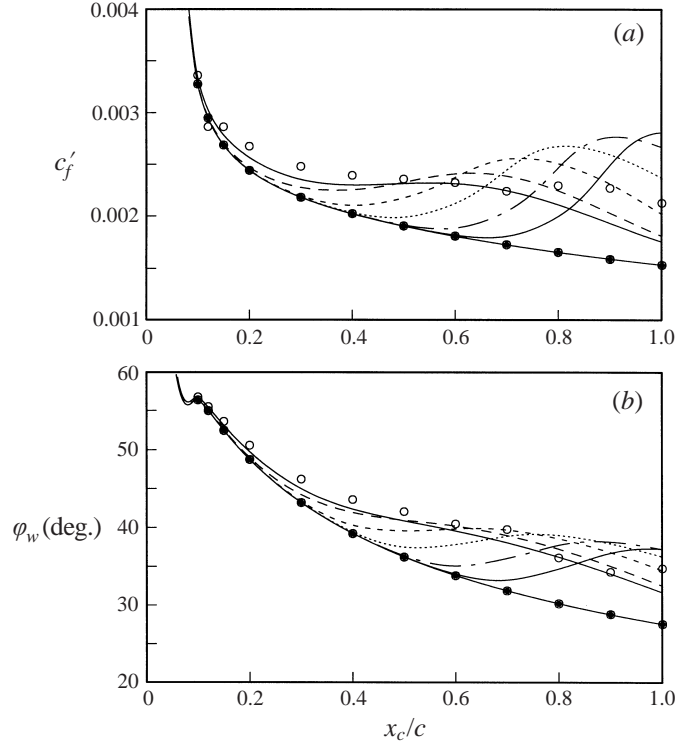


FIGURE 9. Steady crossflow vortices for $\lambda_{z_c}^* = 12$ mm, $Q_{\infty}^* = 19$ m s $^{-1}$ and $\varphi_{\infty} = 42.5^\circ$. Local skin friction factor c'_f (a) and wall streamline angle φ_w (b) as function of chordwise distance x_c/c . The curves correspond to the PSE results of figure 7. The solid circles mark the laminar boundary-layer results while the open circles show the nonlinear equilibrium results with $N_p = 4$.

equilibrium solution and signal the high sensitivity of the flow to the modelling of the mean flow distortion. The bifurcation scenario described above clearly explains the origin of the spatially oscillating solutions and shows that the spatial bifurcation behaviour is analogous to that of temporally oscillating solutions observed in the temporal DNS of Meyer & Kleiser (1988).

For engineering applications the (local) skin friction factor c'_f , defined by

$$c'_f = \frac{\tau_w^*}{\frac{1}{2}\rho^*Q_e^{*2}} \quad \text{with } \tau_w^* = \mu^* \sqrt{\left(\frac{\partial U_{m,c}^*}{\partial y^*}\right)_w^2 + \left(\frac{\partial W_{m,c}^*}{\partial y^*}\right)_w^2},$$

is of vital interest. Here τ_w^* denotes the local wall shear stress with μ^* being the (dynamical) viscosity. The direction of the wall streamline in the chord coordinate system is given by

$$\varphi_w = \arctan \left\{ \left(\frac{\partial W_{m,c}^*}{\partial y^*} \right)_w / \left(\frac{\partial U_{m,c}^*}{\partial y^*} \right)_w \right\}.$$

In figure 9 we show c'_f and φ_w for the PSE results of figure 7 together with the equilibrium solution results. The rather abrupt changes in the laminar results for φ_w near the leading edge are an indication that our model (2.4) for the pressure coefficient is not very realistic in this region. For small x_c/c we have fair agreement between the maximal PSE saturation and the equilibrium Q_{∞} solution. After bifurcation it is only

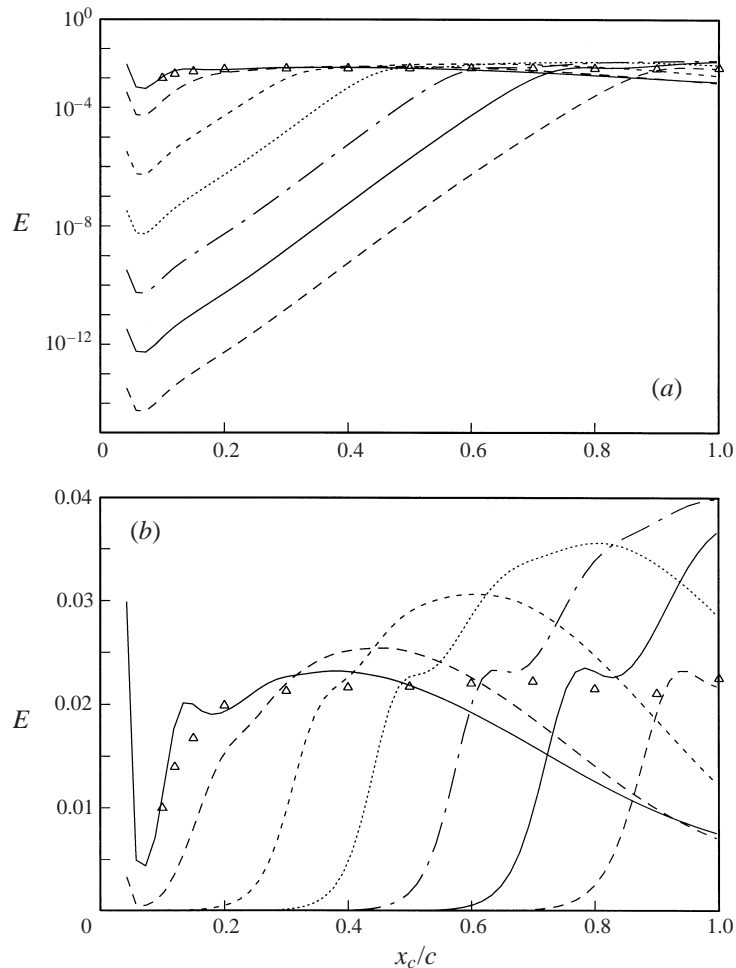


FIGURE 10. Total fluctuation energy E of 135 Hz travelling crossflow vortices as function of chordwise distance x_c/c for $\lambda_{z_c}^* = 12$ mm, $Q_{\infty}^* = 19$ m s $^{-1}$ and $\varphi_{\infty} = 42.5^\circ$: (a) semi-log scale, (b) linear scale. The various curves depict the PSE results for widely varying initial amplitudes. The triangles mark our local 135 Hz equilibrium results of figure 6 with $N_p = 4$.

natural that the two solutions differ. This is in contrast to the fairly smooth equilibrium surface for the fluctuating energy, shown in figure 6, and may be due to our similarity approximation for the mean flow distortion. Figure 9 demonstrates very clearly that an increase of the skin friction does not mean that transition occurred. The strongly nonlinear stationary vortices cause the rapid increase in skin friction, but the flow is still far from being turbulent. It is the instability of this slowly varying stationary vortex which initiates transition. As can be seen in figure 9 the skin friction factor of the equilibrium solutions is often lower than that of the still laminar PSE solution. For fully turbulent flows this is equally true and the unstable equilibrium solutions are sometimes used as goal dynamics in nonlinear control schemes, cf. Keefe (1993).

To see how well our equilibrium solutions approximate the PSE results for travelling waves we also compared the two results for $f^* = 135$ Hz in figure 10, again on a semi-log and linear scale. Note the much lower 'saturation' of the $f^* = 135$ Hz travelling wave compared with the $f^* = 0$ Hz stationary crossflow vortex of figure 7. Now the

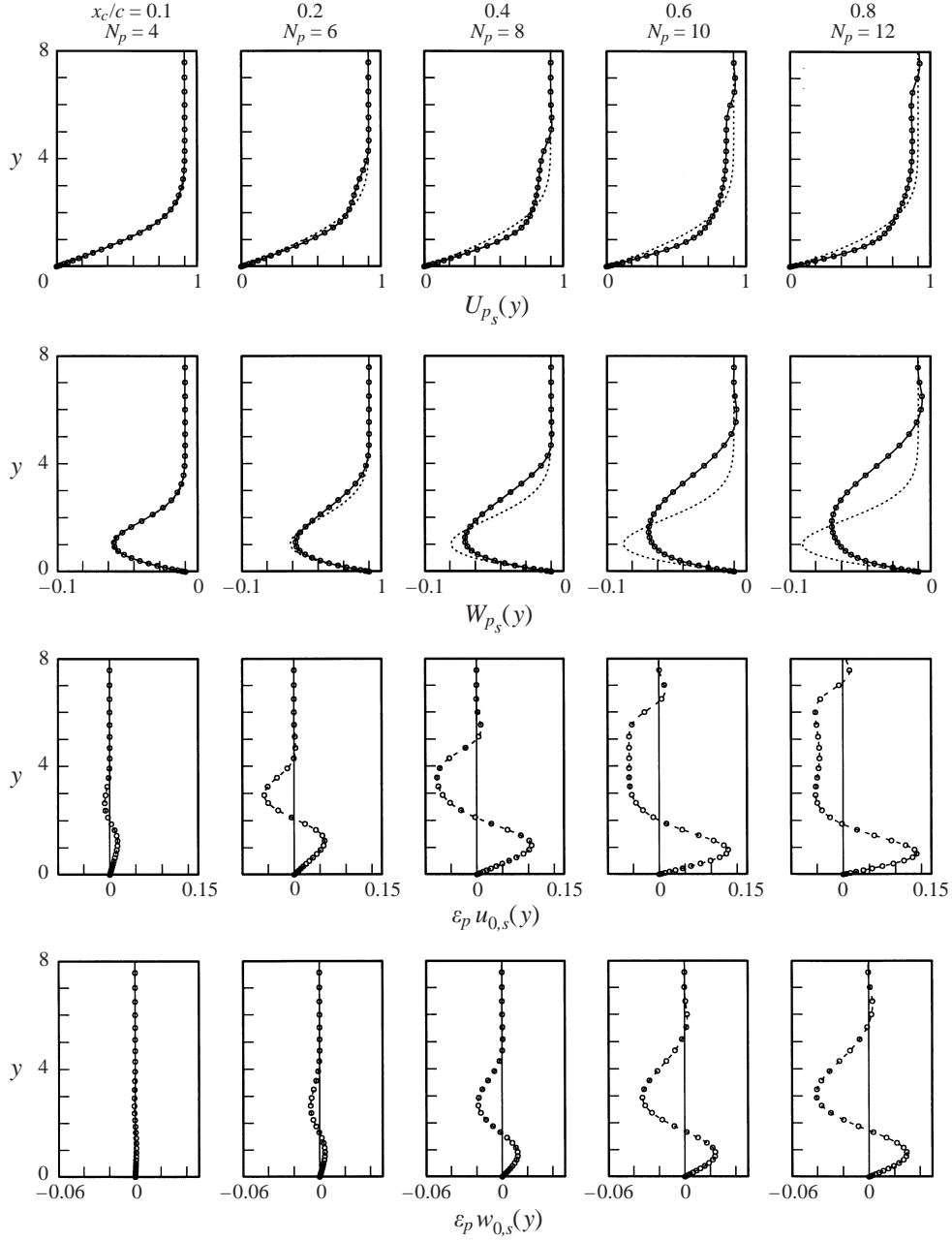


FIGURE 11. Zero-frequency equilibrium solution for $\lambda_{z_c}^* = 12$ mm, $Q_{\infty}^* = 19$ m s⁻¹, $\varphi_{\infty} = 42.5^\circ$ as function of chordwise distance x_c/c : total mean flow velocity profiles $U_{ps}(y)$ and $W_{ps}(y)$ (upper two rows) together with non-similar laminar boundary-layer profiles (dotted curves) and corresponding mean flow distortion profiles $\epsilon_p u_{0,s}(y)$ and $\epsilon_p w_{0,s}(y)$ (lower two rows). $K = 55$ and the Fourier resolution N_p at each x_c/c is as indicated.

equilibrium solution no longer envelopes the PSE results for varying initial amplitudes. The PSE curves seem to ‘hesitate’ near the probably spatially unstable equilibrium solution before saturating at higher amplitudes which probably correspond to a different equilibrium solution. In the following section we describe the zero-frequency

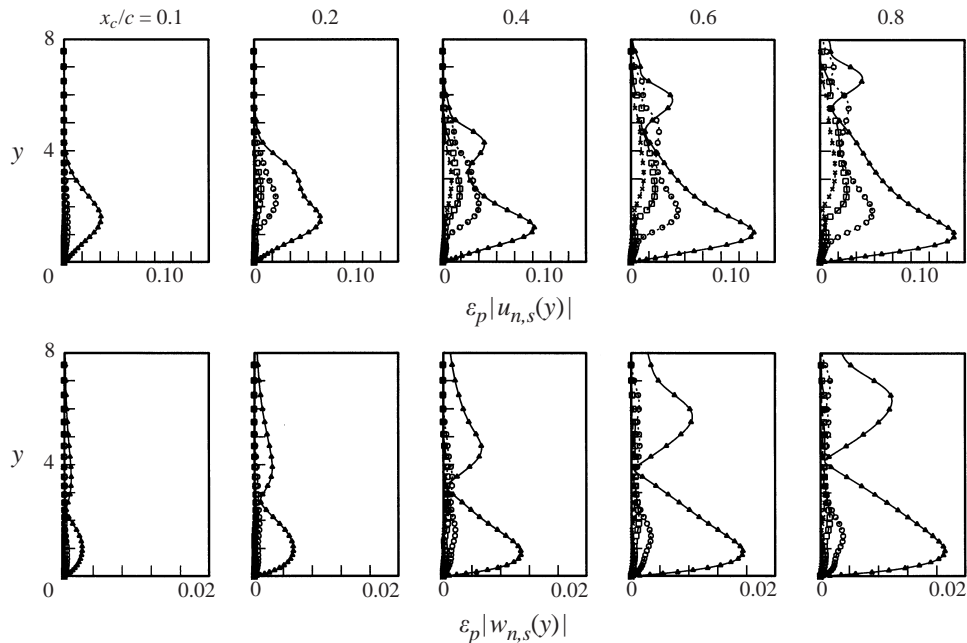


FIGURE 12. Zero-frequency equilibrium solution for $\lambda_{z_c}^* = 12$ mm, $Q_\infty^* = 19$ m s $^{-1}$, $\varphi_\infty = 42.5^\circ$ with N_p as in figure 11: Modal amplitudes $\varepsilon_p |u_{n,s}(y)|$ and $\varepsilon_p |w_{n,s}(y)|$ with $n = 1(\Delta)$, $n = 2(\circ)$, $n = 3(\square)$ and $n = 4(\times)$ corresponding to figure 11.

equilibrium solution in more detail before we use it as nonlinear model flow for our secondary instability investigation in §4.

3.5. Zero-frequency nonlinear equilibrium solution

For the low-turbulence environment encountered in actual flight stationary crossflow vortices are expected to dominate the transition process. The nonlinear zero-frequency equilibrium solution is therefore of particular interest for a study of turbulent breakdown on swept wings and will be described in more detail in this section. Although the low-resolution solution $N_p = 4$ is good enough for the total fluctuation energy E and the friction factor c'_f , the contribution of the higher modes cannot be neglected for certain details of the flow, especially at larger x_c/c . For this reason we increased the number of harmonics N_p up to $N_p = 12$ by means of a local Newton iteration and use these higher resolutions for obtaining the following results.

Figure 11 shows the total mean flow velocity profiles (upper two rows of pictures) of our zero-frequency equilibrium solution in streamwise coordinates together with the corresponding mean flow distortion profiles (lower two rows of pictures) for various chordwise stations x_c/c . The symbols give an idea of the collocation point density. The velocity overshoot of the force-term formulation has disappeared. This seems to be the best we can do for a local solution.

Figure 12 depicts the streamwise and crossflow modal amplitudes for modes $n = 1, \dots, 4$ at various chordwise positions for the zero-frequency equilibrium solution of figure 11. For $x_c/c = 0.1$ the mode $u_{1s}(y)$ is still very similar to the primary eigenfunction and the higher modes are negligible. However, at the $x_c/c = 0.2$ equilibrium $u_{1s}(y)$ has already developed a second maximum near the edge of the boundary layer and the higher modes have to be taken into account. Evidently, the shape assumption

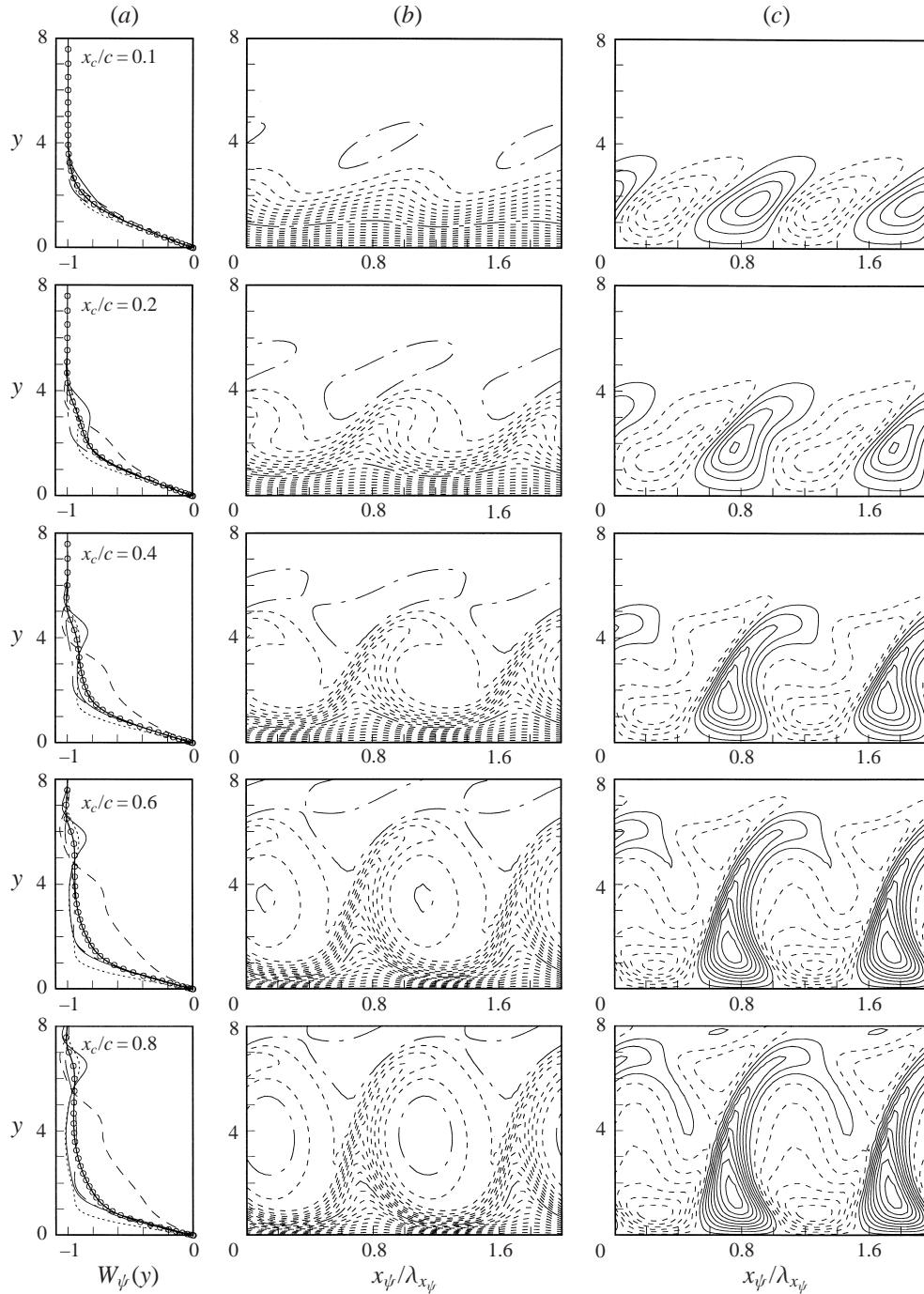


FIGURE 13. Zero-frequency equilibrium solution for $\lambda_{zc}^* = 12 \text{ mm}$, $Q_\infty^* = 19 \text{ m s}^{-1}$, $\varphi_\infty = 42.5^\circ$ with N_p as in figure 11: isolines of the total velocity W_ψ (b) and disturbance velocity $\varepsilon_p \tilde{w}_\psi$ (c) in (x_ψ, y) -plane perpendicular to the axis of the crossflow vortex. Isolines of W_ψ are spaced 0.05 apart with $W_\psi = 0.5$ and 1 marked by dash-dotted lines. Isolines of $\varepsilon_p \tilde{w}_\psi$ are spaced 0.04 apart, starting with 0.02 (except for $x_c/c = 0.1$ which are spaced 0.02 apart, starting with 0.01). Negative values are plotted by dashed lines. (a) The profiles $W_\psi(y)$ at $x_\psi/\lambda_{x_\psi} = 0$ (solid line), 0.25 (dotted), 0.5 (dash dotted) and 0.75 (dashed). The symbols mark the total mean flow.

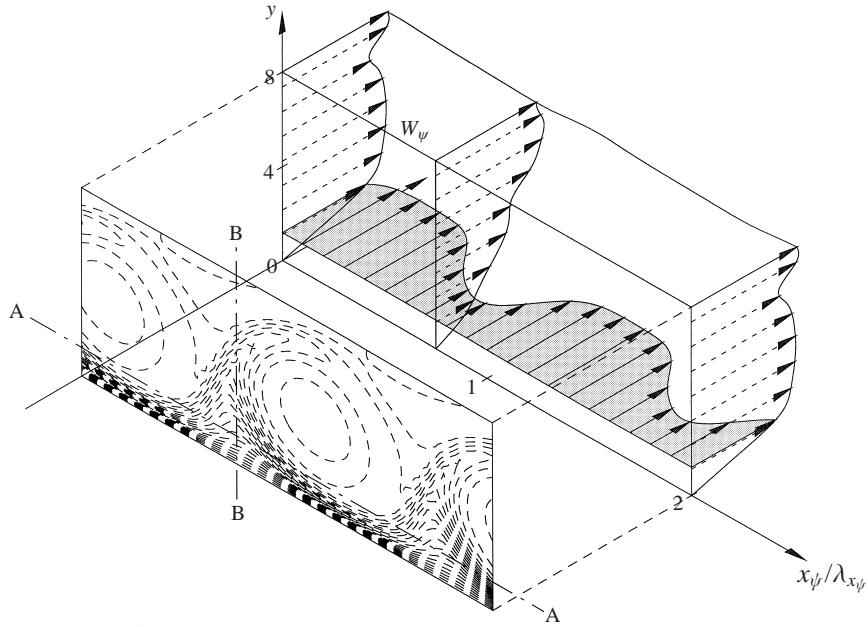


FIGURE 14. Zero-frequency equilibrium solution for $x_c/c = 0.8$ of figure 13: cuts through the spanwise velocity profile $W_\psi(x_\psi)$ at $y = 1.2$ (cut A–A) and the wall-normal velocity profile $W_\psi(y)$ at $x_\psi/\lambda_{x_\psi} = 0.75$ (cut B–B).

is no longer applicable. With increasing downstream distance this second maximum moves further away from the wall and is responsible for the high shear layers causing the high-frequency secondary instabilities near the edge of the boundary layer.

Isolines of the total velocity $W_\psi(x_\psi/\lambda_{x_\psi}, y)$ as well as of the disturbance velocity $\varepsilon_p \tilde{w}_\psi(x_\psi/\lambda_{x_\psi}, y)$ in cuts normal to the axis of the stationary vortex are plotted in figure 13(b, c) for the zero-frequency equilibrium solution of figure 11. Also shown are the velocity profiles $W_\psi(y)$ at four different x_ψ/λ_{x_ψ} -locations together with the total mean flow profile (figure 13a). Various inflection points can be observed in these wall-normal W_ψ profiles. Similarly, the W_ψ velocity profiles also exhibit inflection points in the crossflow direction, as can be seen very clearly for the enhanced $y = 1.2$ cut in figure 14. The secondary high-frequency instabilities, to be investigated in the following section, can be traced to these inflection points and therefore are basically of inviscid nature, cf. Park & Huerre (1995), Li & Malik (1995) or Bottaro & Klingmann (1996) (see also Holmes, Lumley & Berkooz 1996, p. 77 for a discussion of the related bursting phenomenon in low-speed turbulent boundary-layer streaks). Of particular interest is the wake-like appearance of the W_ψ velocity profile, enhanced by the shaded area in figure 14, which makes it quite plausible that an absolute instability could develop just like in wakes behind blunt bodies (see Koch 1985) and be the self-sustaining process leading to the onset of turbulence. This question is still being investigated at present.

4. High-frequency secondary instability

4.1. Governing equations

The nonlinear primary equilibrium solutions of §3 contain strong local shear layers which are the source of the high-frequency inflectional instabilities, see for example

Malik (1986) or Malik *et al.* (1994). An attempt to force the steady crossflow vortices of their PSE solution into breakdown by Wang *et al.* (1994) failed in the absence of any guidance on proper input models. To gain some insight they conducted secondary stability studies. In the following we shall do the same for our nonlinear equilibrium solutions. Two essentially equivalent methods are available, namely Floquet theory, cf. Herbert (1988), or the two-dimensional eigenfunction approach employed by Malik *et al.* (1994). Similarly to Janke & Balakumar (1998a), who very recently performed a Floquet stability analysis for their PSE results on the DLR swept-plate experiment at $x_c/c = 0.6$, we shall also use Floquet theory.

In the wave-oriented coordinate system (x_ψ, y, z_ψ) , cf. figure 2, and in a frame of reference moving with the propagation speed C of the nonlinear equilibrium solution in the x_ψ -direction, the flow can be written

$$\mathbf{q}_\psi(x_\psi, y, z_\psi, t) = \mathbf{Q}_{p_\psi}(x_\psi, y) + \varepsilon \bar{\mathbf{q}}_\psi(x_\psi, y, z_\psi, t). \quad (4.1)$$

Barred quantities denote secondary disturbances. The new base flow is the rotated nonlinear primary equilibrium flow

$$\mathbf{Q}_{p_\psi}(x_\psi, y) = \mathbf{Q}_p(y) + \varepsilon_p \tilde{\mathbf{q}}_{p_\psi}(x_\psi, y) \quad (4.2)$$

which is spatially periodic in the x_ψ -direction with the period $\lambda_{x_\psi} = 2\pi/\alpha_\psi = 2\pi/(\alpha_c^2 + \beta_c^2)^{1/2}$, α_c and β_c being the wavenumbers of the primary equilibrium solution in chordwise coordinates. $\mathbf{Q}_p(y) = \{U_p, 0, W_p\}$ is the rotated quasi-parallel boundary-layer velocity (3.7), (3.8) and

$$\tilde{\mathbf{q}}_{p_\psi}(x_\psi, y) \equiv \left\{ \begin{array}{l} \tilde{u}_{p_\psi}(x_\psi, y) \\ \tilde{v}_p(x_\psi, y) \\ \tilde{w}_{p_\psi}(x_\psi, y) \end{array} \right\} = \sum_{n=-N_p}^{N_p} \left\{ \begin{array}{l} \hat{u}_{n_p}(y) \\ \hat{v}_n(y) \\ \hat{w}_{n_p}(y) \end{array} \right\} e^{in2\pi x_\psi} \quad (4.3)$$

is the rotated primary disturbance velocity.

Substituting (4.1) with (4.2) into the incompressible Navier–Stokes equations and linearizing for $\varepsilon \ll 1$ we obtain the following linear secondary instability equations:

$$\begin{aligned} & \left\{ \frac{\partial}{\partial t} + (U_p - C) \frac{\partial}{\partial x_\psi} + W_p \frac{\partial}{\partial z_\psi} - \frac{1}{Re} \Delta_\psi \right\} \Delta_\psi \bar{v} - \frac{d^2 U_p}{dy^2} \frac{\partial \bar{v}}{\partial x_\psi} - \frac{d^2 W_p}{dy^2} \frac{\partial \bar{v}}{\partial z_\psi} \\ & + \varepsilon_p \left\{ \left[\tilde{u}_{p_\psi} \frac{\partial}{\partial x_\psi} + \tilde{v}_p \frac{\partial}{\partial y} + \tilde{w}_{p_\psi} \frac{\partial}{\partial z_\psi} \right] \Delta_\psi \bar{v} + \frac{\partial \tilde{v}_p}{\partial x_\psi} \frac{\partial \bar{\eta}}{\partial z_\psi} \right. \\ & + \frac{\partial \tilde{u}_{p_\psi}}{\partial x_\psi} \left[\frac{\partial^2 \bar{v}}{\partial x_\psi^2} - \frac{\partial^2 \bar{v}}{\partial y^2} - \frac{\partial^2 \bar{v}}{\partial z_\psi^2} - 2 \frac{\partial^2 \bar{u}_p}{\partial x_\psi \partial y} \right] + \frac{\partial \tilde{\xi}_{p_\psi}}{\partial x_\psi} \left[\frac{\partial \bar{v}}{\partial y} + 2 \frac{\partial \bar{u}_p}{\partial x_\psi} \right] \\ & + \frac{\partial^2 \tilde{\xi}_{p_\psi}}{\partial x_\psi^2} \bar{u}_p + \frac{\partial \tilde{\xi}_{p_\psi}}{\partial y} \frac{\partial \bar{v}}{\partial x_\psi} + \frac{\partial^2 \tilde{\xi}_{p_\psi}}{\partial x_\psi \partial y} \bar{v} + \frac{\partial \tilde{v}_p}{\partial x_\psi} \left[\frac{\partial^2 \bar{v}}{\partial x_\psi \partial y} - \frac{\partial^2 \bar{u}_p}{\partial y^2} \right] \\ & \left. - 2 \tilde{\eta}_p \left[\frac{\partial^2 \bar{v}}{\partial x_\psi \partial z_\psi} - \frac{\partial^2 \bar{u}_p}{\partial y \partial z_\psi} \right] - 2 \frac{\partial \tilde{\xi}_{p_\psi}}{\partial x_\psi} \frac{\partial \bar{u}_p}{\partial z_\psi} - \left[\frac{\partial \tilde{\eta}_p}{\partial x_\psi} + \frac{\partial \tilde{\xi}_{p_\psi}}{\partial y} \right] \frac{\partial \bar{v}}{\partial z_\psi} \right\} = 0, \quad (4.4) \end{aligned}$$

$$\begin{aligned} & \left\{ \frac{\partial}{\partial t} + (U_p - C) \frac{\partial}{\partial x_\psi} + W_p \frac{\partial}{\partial z_\psi} - \frac{1}{Re} \Delta_\psi \right\} \bar{\eta} + \frac{dU_p}{dy} \frac{\partial \bar{v}}{\partial z_\psi} - \frac{dW_p}{dy} \frac{\partial \bar{v}}{\partial x_\psi} \\ & + \varepsilon_p \left\{ \tilde{u}_{p_\psi} \frac{\partial \bar{\eta}}{\partial x_\psi} + \tilde{v}_p \frac{\partial \bar{\eta}}{\partial y} + \tilde{w}_{p_\psi} \frac{\partial \bar{\eta}}{\partial z_\psi} - \frac{\partial \tilde{v}_p}{\partial x_\psi} \bar{\xi}_\psi - \frac{\partial \tilde{v}_p}{\partial y} \bar{\eta} \right. \\ & \left. + \frac{\partial \tilde{\eta}_p}{\partial x_\psi} \bar{u}_p + \frac{\partial \tilde{\eta}_p}{\partial y} \bar{v} - \bar{\xi}_{p_\psi} \frac{\partial \bar{v}}{\partial x_\psi} - \tilde{\eta}_p \frac{\partial \bar{v}}{\partial y} - \bar{\xi}_{p_\psi} \frac{\partial \bar{v}}{\partial z_\psi} \right\} = 0. \quad (4.5) \end{aligned}$$

Here Δ_ψ denotes the Laplacian and $\{\tilde{\xi}_{p_\psi}, \tilde{\eta}_p, \tilde{\zeta}_{p_\psi}\}$ are the Cartesian components of the primary disturbance vorticity vector in the wave coordinate system. The continuity equation together with the definition of vorticity complete the system of governing equations. The solution has to satisfy the no-slip boundary conditions on the plate and vanishes as $y \rightarrow \infty$. For a two-dimensional nonlinear base flow $\{U_\psi + \tilde{u}_{p_\psi}, \tilde{v}_p\}$ with $W_\psi = \tilde{w}_{p_\psi} = \tilde{\xi}_{p_\psi} = \tilde{\eta}_p = 0$, equations (4.4) and (4.5) reduce to those in Koch (1992).

The coefficients of equations (4.4) and (4.5) are periodic in x_ψ but independent of z_ψ and t . Using the normal-mode concept and applying Floquet theory, cf. Herbert (1988), the solution can be expressed in the form

$$\begin{Bmatrix} \bar{v} \\ \bar{\eta} \end{Bmatrix} (x_\psi, y, z_\psi, t) = e^{\sigma t + i(a_\psi x_\psi + b_\psi z_\psi)} \sum_{v=-\infty}^{\infty} \begin{Bmatrix} \bar{v}_v(y) \\ \bar{\eta}_v(y) \end{Bmatrix} e^{iv\alpha_\psi x_\psi}. \quad (4.6)$$

Here $a_\psi = a_{\psi,r} + ia_{\psi,i}$ is the (complex) Floquet exponent and b_ψ is real and prescribed. In our temporal approach the spatial growth rate $-a_{\psi,i}$ is zero and the detuning $a_{\psi,r}$ of the primary wavenumber α_ψ is prescribed (usually $a_{\psi,r}$ is replaced by $\delta = a_{\psi,r}/\alpha_\psi$ such that $0 \leq \delta < 1$). $\sigma = \sigma_r + i\sigma_i$ is the complex eigenvalue with σ_r giving the temporal growth rate and σ_i being the frequency shift of the secondary instability. The corresponding (dimensional) frequency shift is

$$f^* [\text{Hz}] = \frac{\sigma_i Q_{ref}^*}{2\pi L_{ref}^*}.$$

Substituting (4.6) and (4.3) into equations (4.4) and (4.5) and collecting terms with the same Fourier exponent we obtain a system of ODEs governing the secondary instability modes $(\bar{v}_n, \bar{\eta}_n)$ with $-N_s \leq n \leq +N_s$ (in general $N_s \geq N_p$)

$$\begin{aligned} & \left\{ \frac{1}{Re} \left(\frac{d^2}{dy^2} - [(n+\delta)^2 \alpha_\psi^2 + b_\psi^2] \right)^2 - [i(n+\delta)\alpha_\psi(U_\psi - C) + ib_\psi W_\psi + \sigma] \right. \\ & \quad \times \left. \left(\frac{d^2}{dy^2} - [(n+\delta)^2 \alpha_\psi^2 + b_\psi^2] \right) + i(n+\delta)\alpha_\psi \frac{d^2 U_\psi}{dy^2} + ib_\psi \frac{d^2 W_\psi}{dy^2} \right\} \bar{v}_n \\ & \quad - \varepsilon_p \sum_{v=-N_p}^{N_p} S_{n-v,v}^{OS} = 0, \end{aligned} \quad (4.7)$$

$$\begin{aligned} & \left\{ \frac{1}{Re} \left(\frac{d^2}{dy^2} - [(n+\delta)^2 \alpha_\psi^2 + b_\psi^2] \right) - i(n+\delta)\alpha_\psi(U_\psi - C) - ib_\psi W_\psi - \sigma \right\} \bar{\eta}_n \\ & \quad - i \left\{ b_\psi \frac{dU_\psi}{dy} - (n+\delta)\alpha_\psi \frac{dW_\psi}{dy} \right\} \bar{v}_n - \varepsilon_p \sum_{v=-N_p}^{N_p} S_{n-v,v}^{SQ} = 0. \end{aligned} \quad (4.8)$$

With $\mu = n - v$ the equation of continuity together with the definition of vorticity can be used to eliminate $\bar{u}_\mu, \bar{w}_\mu, \bar{\xi}_\mu, \bar{\zeta}_\mu$ in terms of \bar{v}_μ and $\bar{\eta}_\mu$ such that the right-hand-side convolution terms can be written

$$S_{\mu,v}^{OS} = A_{\mu,v}^{OS} \bar{v}_\mu + B_{\mu,v}^{OS} \frac{d\bar{v}_\mu}{dy} + C_{\mu,v}^{OS} \frac{d^2 \bar{v}_\mu}{dy^2} + D_{\mu,v}^{OS} \frac{d^3 \bar{v}_\mu}{dy^3} + E_{\mu,v}^{OS} \bar{\eta}_\mu + F_{\mu,v}^{OS} \frac{d\bar{\eta}_\mu}{dy} + G_{\mu,v}^{OS} \frac{d^2 \bar{\eta}_\mu}{dy^2}, \quad (4.9)$$

$$S_{\mu,v}^{SQ} = A_{\mu,v}^{SQ} \bar{v}_\mu + B_{\mu,v}^{SQ} \frac{d\bar{v}_\mu}{dy} + C_{\mu,v}^{SQ} \frac{d^2 \bar{v}_\mu}{dy^2} + D_{\mu,v}^{SQ} \bar{\eta}_\mu + E_{\mu,v}^{SQ} \frac{d\bar{\eta}_\mu}{dy}. \quad (4.10)$$

The coefficients $A_{\mu,v}^{OS}, \dots$ are functions of the primary equilibrium solution, truncated at $v = \pm N_p$, and are listed for reference in the Appendix. For a two-dimensional nonlinear base flow they reduce to the ones presented in Koch (1992).

4.2. Numerical solution procedure

For the numerical computation of the (temporal) eigenvalues σ , equations (4.7) and (4.8) are discretized in wall-normal direction via Chebyshev collocation. In order to provide adequate resolution near the boundary-layer edge, where the maxima of the most amplified secondary eigenfunctions are expected, the physical domain $y \in [0, \infty)$ is mapped into a single Chebyshev domain $\chi \in [1, 0)$ by a convolution of two mappings originally introduced by Erlebacher & Hussaini (1990). First, the hyperbolic-tangent mapping

$$\psi + t_\varepsilon \tanh [(\psi - \psi_{crit})/\Delta\psi_{crit}] = (\chi - \chi_{crit})/\Delta\chi_{crit}$$

takes χ to an intermediate variable ψ , concentrating nodes about ψ_{crit} (in our secondary stability computation we concentrate nodes in general near the boundary-layer edge $y_{crit} = \delta_{99.9}$, where the boundary-layer thickness $\delta_{99.9}$ is defined as the wall-normal distance at which the streamwise velocity of the laminar base flow reaches 99.9% of its free-stream value). The width of the concentration region is fixed by $\Delta\psi_{crit}$ while t_ε is a measure for the influence of the hyperbolic redistribution term. The second exponential mapping

$$\psi = e^{-y/y_0}$$

maps ψ onto the physical variable y . The resulting generalized algebraic eigenvalue problem can then be solved by an efficient global solver to obtain the whole or part of the eigenvalue spectrum. Despite the v - η formulation our eigenvalue problem is of rather large order (2000 and more, depending on how many modes are retained) such that traditional eigenvalue solvers like the QR or QZ algorithm become rather time intensive and are used only for selected tests. The *shift-and-invert Arnoldi algorithm*[†], cf. Saad (1992) or Nayar & Ortega (1993), is highly efficient for obtaining the most unstable part of the spectrum. Once a fairly good estimate of a particular eigenvalue has been found, we use the local *Wielandt iteration*[‡] for refining the eigenvalue.

Figure 15 depicts a typical global secondary eigenvalue spectrum. For each retained secondary mode $-N_s \leq n \leq +N_s$ a (numerically approximated) continuous spectrum appears in $\sigma_r \leq 0$, but of particular interest are the amplified discrete modes with $\sigma_r > 0$. Varying N_s but keeping $K_s = 55$ constant, we confirm the findings of previous investigators, see for example Balachandar *et al.* (1992), Malik *et al.* (1994) or Wang *et al.* (1994), namely that many more secondary modes have to be retained to obtain reasonably converged results than in a secondary stability analysis of two-dimensional boundary layers. It appears that under-resolution (of the primary base flow as well as of the secondary stability analysis) not only gives numerically wrong amplification rates but also is the source of additional amplified modes. In our computation we retained $N_s \geq N_p$ modes, where N_p is the number of primary modes retained in the computation of the primary equilibria, cf. figure 11.

While there are negligible variations if K_s is increased to $K_s = 75$ with the mapping fixed, the results are quite sensitive if not enough wall-normal collocation points are

[†] We are indebted to U. Ehrenstein who brought this method to our attention and even let us use his version of the algorithm.

[‡] We are grateful to Th. Herbert who pointed out this classical method and sent us the corresponding reference (Zurmühl 1961, p. 289ff).

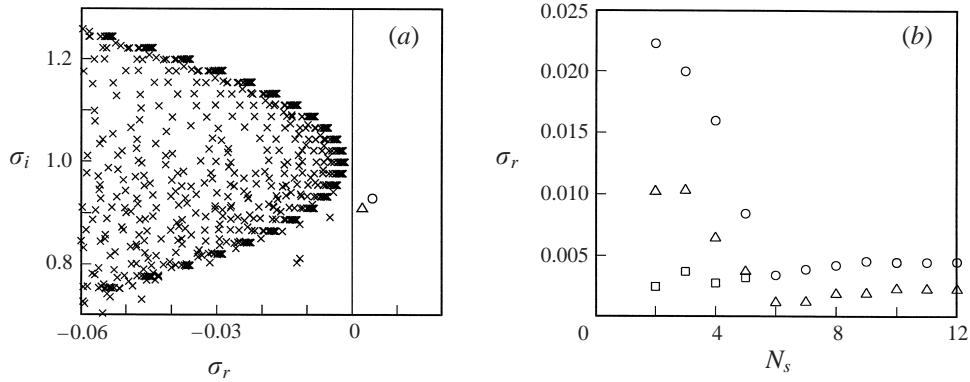


FIGURE 15. (Temporal) secondary stability of zero-frequency equilibrium solution at $x_c/c = 0.4$ with $N_p = 8$: (a) global eigenvalue spectrum at $b_\psi = 1$ with $N_s = 12, K_s = 55$ and $\delta = 0$; (b) variation of amplification rate σ_r of the highest amplified modes (O, most amplified mode; Δ , second most amplified mode) with N_s keeping $K_s = 55$ constant.

near the maxima of the eigenfunction. For higher frequencies these maxima are a large distance away from the wall which can lead to under-resolution. Here a multi-domain method would have been preferable to the two-step mapping used in our secondary stability computation.

4.3. Selected temporal secondary stability results

In this section we present some temporal secondary stability results for the zero-frequency nonlinear equilibrium solution of § 3.5 at various fixed locations x_c/c . At each location we vary b_ψ , the wavenumber in the direction of the primary vortex axis, and observe the change in the temporal growth rate σ_r .

First we set the detuning parameter $\delta = 0$. After the nonlinear equilibrium solution reaches a (relatively high) threshold amplitude somewhere between $x_c/c = 0.15$ and $x_c/c = 0.2$ a single unstable high-frequency secondary mode appears. At $x_c/c = 0.2$ it reaches the same growth rate as the corresponding primary instability at zero amplitude. The iso-amplitude curves of this secondary instability mode correlate with the spanwise shear of $W_\psi(x_\psi)$. Therefore, this mode belongs to the ‘mode I’ family of Malik *et al.* (1996). Proceeding to higher x_c/c , and therefore higher amplitudes of the equilibrated primary crossflow vortex, well over ten modes become unstable over a much wider range of unstable wavenumbers b_ψ . The corresponding frequencies, which for each mode are nearly proportional to b_ψ , also increase. Figure 16 depicts the situation for $x_c/c = 0.4$. The most amplified secondary mode with a frequency of $f^* = 1070$ Hz and a wavelength $\lambda_{z_\psi}^* = 11.49$ mm at its maximum is again of the ‘mode I’ type and its growth rate versus b_ψ is shown by the solid line. For comparison, the shaded area in the figure marks the growth rate of the primary instability as function of $\beta_\psi = b_\psi$.

There are two more unstable modes with almost equally high amplification which are clearly of the ‘mode II’ type. According to Malik *et al.* (1996) the amplitude of this mode type can be associated with the wall-normal shear of $W_\psi(y)$ near the edge of the boundary layer seen as a little dip in the local $W_\psi(y)$ velocity profile at $x_\psi/\lambda_{x_\psi} = 0$ of figure 13. We depict the growth rate of ‘mode II’-type instabilities by dashed lines. At its maximum one mode II has a frequency of $f^* = 2392$ Hz and a wavelength of $\lambda_{z_\psi}^* = 6.34$ mm while the second mode II has a frequency of $f^* = 2849$ Hz and

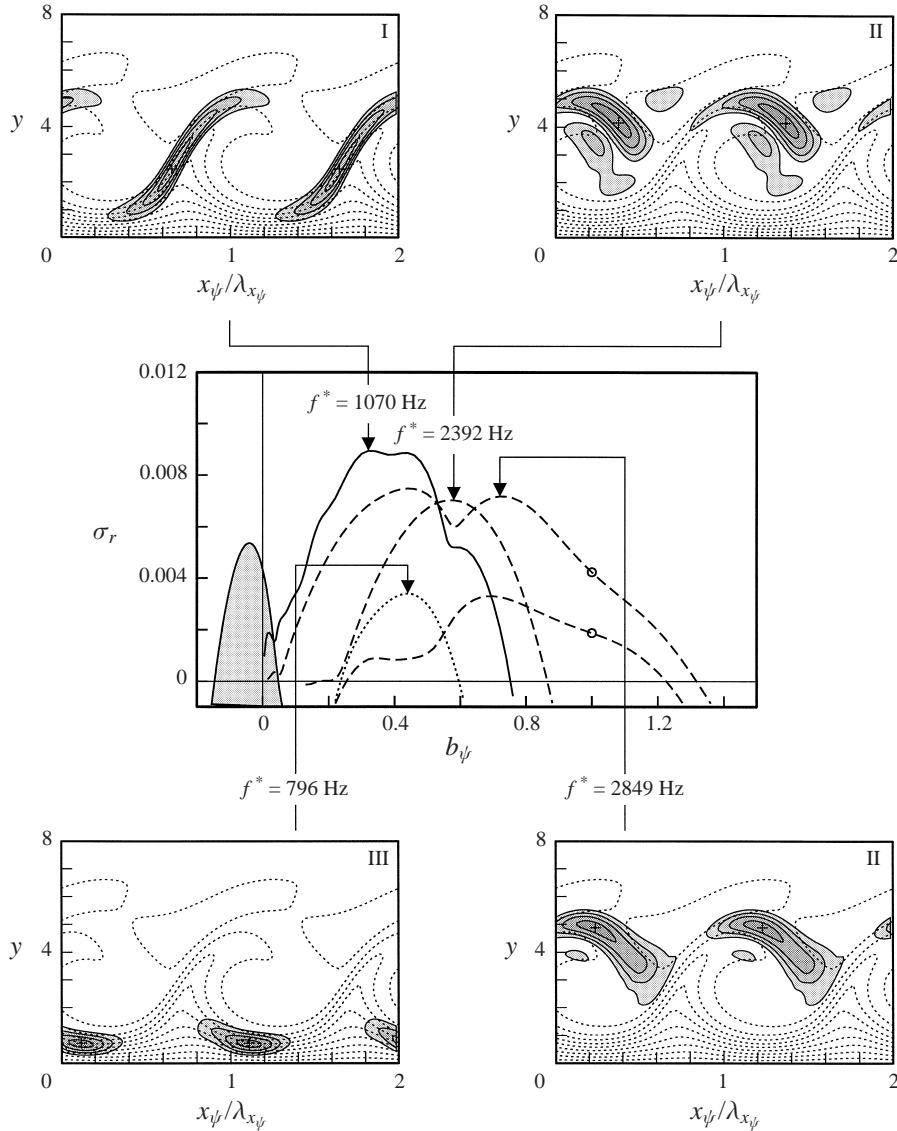


FIGURE 16. Temporal growth rate σ_r of secondary instability modes versus wavenumber b_ψ at $x_c/c = 0.4$ with $N_s = N_p = 8, K = 55$. Also shown are iso-amplitude plots $|\bar{w}_\psi|/\max|\bar{w}_\psi| = 0.3, 0.5, 0.7, 0.9$ of the normalized secondary eigenfunctions corresponding to the four most amplified modes superimposed on the (dotted) isolines of the total velocity W_ψ of figure 13.

a wave length of $\lambda_{z_\psi}^* = 5.10$ mm. The amplitude of a third type of mode (shown by the dotted curve and termed ‘mode III’), with a lower growth rate and a frequency of $f^* = 796.2$ Hz and $\lambda_{z_\psi}^* = 8.35$ mm at its maximum, can be correlated with the wall-normal shear of $W_\psi(y)$ near the wall and therefore seems to correspond to the instability modes found by the early investigators which used the shape assumption, cf. for example Fischer *et al.* (1993). Figure 16 contains iso-amplitude plots of the four most amplified eigenfunctions, superimposed on the isolines of the total velocity W_ψ of figure 13. The eigenfunctions are normalized with the maximal amplitude in

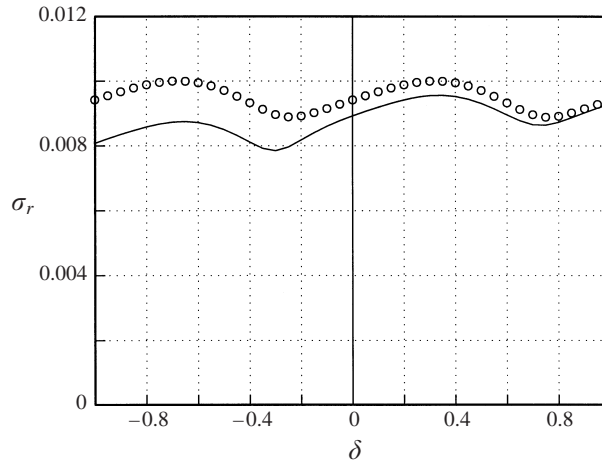


FIGURE 17. Temporal growth rate σ_r of the most amplified secondary instability mode at $x_c/c = 0.4, b_\psi = 0.32$ versus detuning parameter $-1 \leq \delta \leq +1$ with $K = 55$ and $N_p = 8$. The solid curve shows the results for $N_s = 8$ while the symbols mark the results for $N_s = 12$.

the field, the location of which is marked by a cross in the iso-amplitude plots. These contour plots clearly link the modal amplitude with the corresponding shear layer and allow the mode classification used above. The two circles in figure 16 at $b_\psi = 1$ mark the results for $N_s = 8$ of figure 15 which gives an indication of the convergence of a type II mode.

For a further test of convergence we compare the rate of amplification of the most amplified mode at $\delta = 0$ with that at $\delta = \pm 1$. Because this shift only amounts to renumbering the harmonics in equation (4.6) a fully converged solution should give identical results for detuning parameters δ which differ by an integer. As can be seen clearly in figure 17 the $N_s = 8$ results are not yet fully converged while the $N_s = 12$ results, marked by symbols, give the same eigenvalue at $\delta = \pm 1$ and $\delta = 0$. However, the difference at $\delta = 0$ is small so that we retain in general only $N_s = N_p$ modes in our secondary stability analysis. Yet, the asymmetry is apparent. This suggests that an asymmetric truncation of n in equations (4.7) and (4.8) as in Fischer & Dallmann (1991) could be used. At the same time figure 17 demonstrates the almost negligible influence of the detuning parameter δ on σ_r for the most amplified mode at $x_c/c = 0.4, b_\psi = 0.32$ (similarly to the rotating disk results of Balachandar *et al.* 1992). Therefore we limit our parametric investigation in the following to the fundamental resonance case $\delta = 0$.

We computed the temporal secondary instability at various locations x_c/c and figure 18 summarizes the results for the modes with highest amplification. All 'mode I'-type modes are shown by solid curves and 'mode II'-type modes are depicted by dashed curves. Again the shaded area in the left figures marks the growth rate of the primary instability as a function of $\beta_\psi = b_\psi$ for comparison. For the most amplified mode an iso-amplitude plot, superimposed on the isolines of the total velocity W_ψ , clearly shows which shear layer is responsible for this instability. We observe that beginning at a threshold (somewhere between $x_c/c = 0.15$ and $x_c/c = 0.2$) the 'mode I' type instability, caused by inflection points in the spanwise velocity profile $W_\psi(x_\psi)$, dominates the secondary instability of our equilibrated crossflow vortex, especially at higher amplitudes of the primary vortex. This agrees with the findings

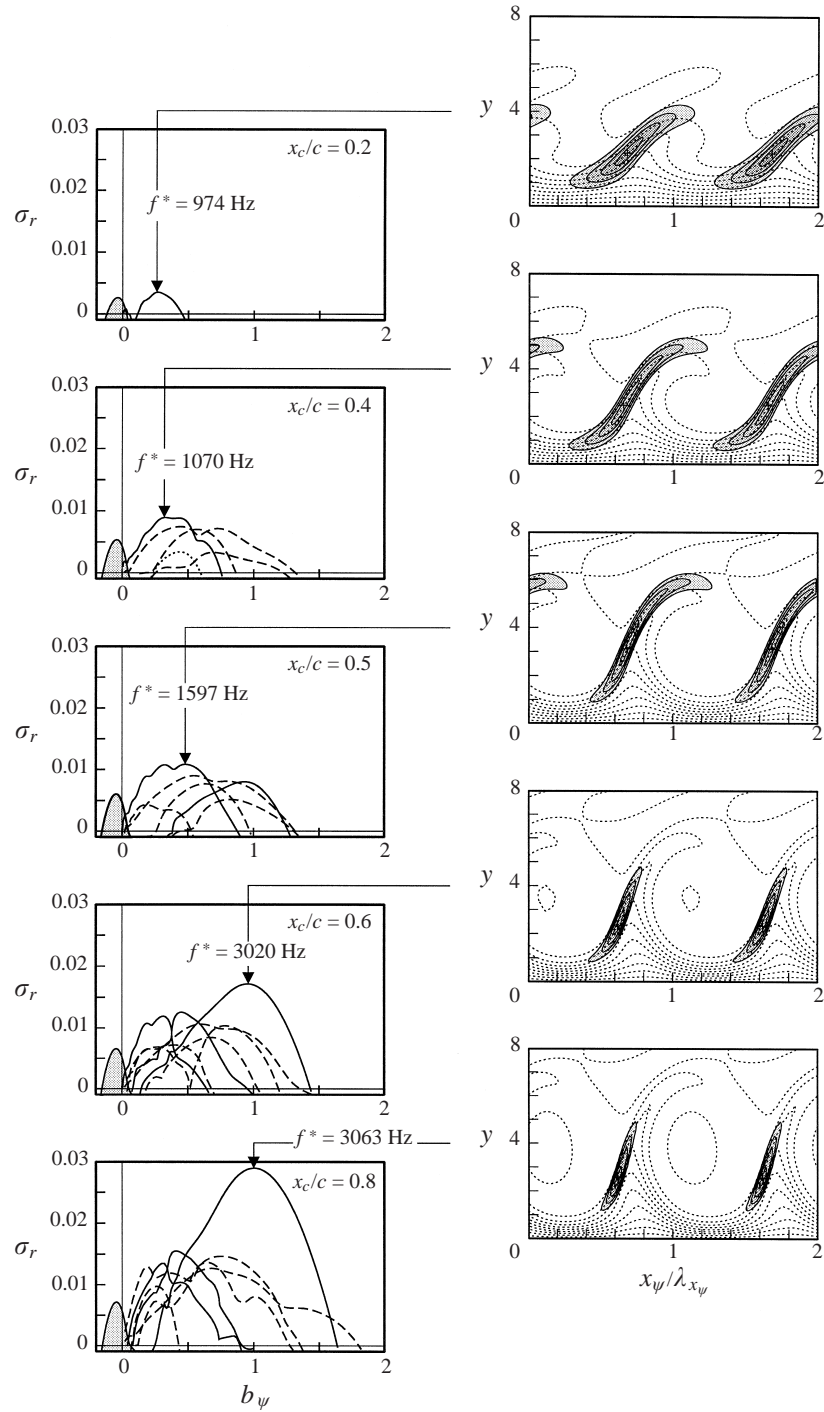


FIGURE 18. Temporal growth rate σ_r of secondary instability modes versus wavenumber b_ψ at various x_c/c with $N_s = N_p$ as indicated in figure 11. Also shown are iso-amplitude plots of $|\bar{w}_\psi|/\max|\bar{w}_\psi|$ of the normalized secondary eigenfunction corresponding to the most amplified mode superimposed on the (dotted) isolines of the total velocity W_ψ of figure 13.

of Högberg & Henningson (1998) for random frequency disturbances in their spatial DNS simulation of the DLR swept-plate experiment at $x_c/c = 0.538$ as well as the recent experimental observations of Kawakami, Kohama & Okutsu (1999). For the Arizona State University swept wing at 45% chord Malik *et al.* (1996) also identified the ‘mode I’-type instability as the most dangerous one. Similarly, the most amplified mode in the investigation of Janke (1998) of the DLR swept-plate experiment at chordwise station $x_c/c = 0.6$ is also a ‘type I’ mode. However, in their paper these authors discuss mainly the modal coincidence of two ‘type II’ modes with lower amplification.

From figure 18 we see that up to about $x_c/c = 0.5$ a type I mode with a frequency of approximately 1000 Hz is the most amplified mode, but modes of type II have almost the same amplification. At $x_c/c = 0.5$ a second type I mode, with a frequency of approximately 3000 Hz, emerges (probably after a modal coalescence) and becomes the dominating amplified mode for $x_c/c > 0.5$. Using a PSE primary base flow instead of our equilibrium solution Stolte (1999) found a similar dominance at higher amplitudes. While at $x_c/c = 0.2$ only a single high-frequency mode is amplified, more than 10 modes with $\sigma_r > 0$ exist for larger x_c/c . At $x_c/c = 0.6$ we observe that a third ‘type I’ mode is just about to coalesce with the first ‘type I’ mode near $b_v = 0.378$. Such a modal coalescence was a focus in the work of Janke & Balakumar (1998*a*), who termed it erroneously an absolute instability but corrected their statement in the forthcoming publication Janke & Balakumar (1998*b*). For an absolute instability to exist the ‘pinching criterion’ of Briggs (1964), with the extension to spatially periodic flows by Brevdo & Bridges (1996), has to be satisfied. A modal coalescence of modes propagating in the same direction, see for example Koch (1992), only implies locally algebraic growth. However, the existence of apparently many such modal coalescences makes it extremely difficult to decide which one, if any, might be of importance for transition. A search for a true absolutely unstable secondary instability, at present under investigation, might shed some light on the breakdown process.

4.4. *Relation between temporal and spatial growth rates of secondary instabilities*

If such an absolute instability exists, the temporal approach would be the correct one. However, at their initiation secondary instabilities of crossflow vortices appear to be convective instabilities, and therefore a spatial secondary stability analysis is more appropriate. The usual global companion-matrix approach, cf. Bridges & Morris (1984), leads to storage requirements which are beyond the capacity of our workstation. We therefore derive in this section an extension of Gaster’s (1962) transformation for secondary instabilities and test its accuracy by computing a few spatial points by local iteration. Gaster’s (1962) well-known transformation, together with the extension to non-parallel flows by Nayfeh & Padhye (1979), relates the spatial growth rate to the temporal growth rate for primary instabilities via the group velocity c_g . For the case of the Falkner–Skan family of boundary-layer profiles Bertolotti (1985) presented the corresponding relation for a secondary instability. He showed that both the phase velocity C of the primary instability as well as the group velocity c_g of the secondary instability are involved in the transformation. For $C \rightarrow 0$ he recovered Gaster’s result. Here we extend this spatial–temporal relation to three-dimensional flows that are uniform in the spanwise coordinate z_c (infinite-swept-wing condition). Such a relation is useful, for example, in relating temporal growth rates for the secondary instabilities, or temporal DNS results in general, to experimental results.

The swept-wing spatial growth problem is easiest to formulate in the chordwise

coordinate system, in which the secondary instability disturbance (4.6) takes the form

$$\left\{ \begin{array}{l} \bar{v} \\ \bar{\eta} \end{array} \right\} (x_c, y, z_c, t) = e^{\sigma t + i(a_c x_c + b_c z_c)} \sum_{v=-\infty}^{\infty} \left\{ \begin{array}{l} \bar{v}_v(y) \\ \bar{\eta}_v(y) \end{array} \right\} e^{iv(\alpha_c x_c + \beta_c z_c)}. \quad (4.11)$$

Here α_c, β_c are the (real) wavenumbers characterizing the primary equilibrium solution, and a_c, b_c are the corresponding (complex) wavenumbers of the secondary instability. The homogeneity in z_c of the mean flow implies that the spanwise wavenumber b_c is a complex constant. We allow no spatial growth in the spanwise direction and therefore take b_c to be a real constant. The solution (4.11) describes the secondary instability disturbance in the Galilean coordinate system moving with C in the x_p -direction, which makes the primary equilibrium solution steady. However, spatial growth rates in the experiment are measured in the fixed laboratory coordinate system in which the primary equilibrium solution oscillates in time with the frequency $\omega = kC$, where $k = (\alpha_c^2 + \beta_c^2)^{1/2}$ is the magnitude of the primary wavenumber in the x_p -direction. Therefore, in the laboratory-fixed coordinate system (denoted by the subscript L) the temporal exponent of (4.11) is

$$\sigma_L = \sigma - ia_c C \cos \psi_c - ib_c C \sin \psi_c.$$

The solution of the eigenvalue problem associated with (4.11) leads to a dispersion relation involving σ, a_c and b_c , or equivalently $a_c = a_c(\sigma, b_c)$, where we assume a_c to be an analytic function of σ and b_c . Following Gaster's (1962) procedure we construct a path in the (σ, b_c) -plane connecting the two end points corresponding to temporal and spatial growth:

$$\begin{aligned} \text{Temporal growth: } a_{c,i}^{(t)} = 0 &\longrightarrow \sigma_r = \sigma_r^{(t)} = \sigma_{L,r}^{(t)}, \\ \text{Spatial growth: } \sigma_{L,r}^{(s)} = 0 &\longrightarrow a_{c,i} = a_{c,i}^{(s)}, \quad \sigma_r^{(s)} = -a_{c,i}^{(s)} C \cos \psi_c. \end{aligned}$$

Here $\sigma_r^{(t)}$ and $-a_{c,i}^{(s)}$ denote the temporal and spatial growth rate, respectively. The spatial and temporal end points correspond to the same mode and therefore have the same frequency in the laboratory-fixed coordinate system. Since b_c is a constant, we can drop the b_c dependence and use σ_r to parameterize the path. Making use of the Cauchy–Riemann relations

$$\frac{\partial a_{c,r}}{\partial \sigma_r} = \frac{\partial a_{c,i}}{\partial \sigma_i}, \quad \frac{\partial a_{c,i}}{\partial \sigma_r} = -\frac{\partial a_{c,r}}{\partial \sigma_i},$$

we obtain the spatial growth rate $a_{c,i}^{(s)}$ by integrating the second relation with respect to σ_r from state (t) to state (s)

$$a_{c,i}^{(s)} = - \int_{\sigma_r^{(t)}}^{\sigma_r^{(s)}} \frac{\partial a_{c,r}}{\partial \sigma_i} d\sigma_r. \quad (4.12)$$

This is the desired relation between spatial and temporal growth. When the integrand remains essentially constant along the integration path, an approximate expression is obtained by expanding the integrand in a Taylor series about the temporal end point, i.e.

$$\frac{\partial a_{c,r}}{\partial \sigma_i} = \frac{\partial a_{c,r}}{\partial \sigma_i} \Big|_{\sigma_r = \sigma_r^{(t)}} + \frac{\partial^2 a_{c,r}}{\partial \sigma_i^2} \Big|_{\sigma_r = \sigma_r^{(t)}} (\sigma_r - \sigma_r^{(t)}) + \dots \quad (4.13)$$

The first term in the Taylor series is the negative inverse of the group velocity in the chord direction, $c_g = -\partial \sigma_i / \partial a_{c,r}$, evaluated at the temporal end point. The group velocity in the spanwise direction z_c is zero since b_c is a constant. Truncating the

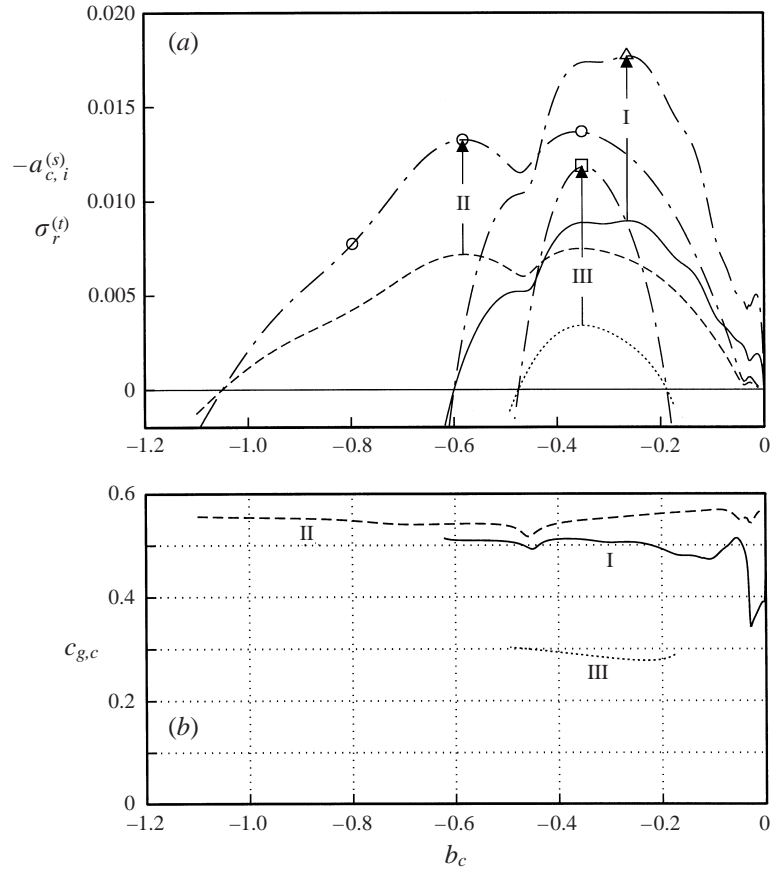


FIGURE 19. (a) Comparison of temporal growth rates $\sigma_r^{(t)}$ with spatial growth rates $-a_{c,i}^{(s)}$ of the three secondary instability mode types I, II and III of figure 16 (with $x_c/c = 0.4$) as function of spanwise wavenumber b_c . The spatial growth rates, obtained by (4.14), are depicted by dash-dotted curves and the arrows connect the temporal curves with the corresponding spatial curves. The symbols mark a few 'exact' spatial growth rates obtained by local iteration. (b) The group velocities $c_{g,c}$ in the chord direction for the three modes.

series expansion (4.13) after the first term and substituting it into (4.12) yields the following approximate relation:

$$a_{c,i}^{(s)} = -\frac{\sigma_r^{(t)}}{c_g + C \cos \psi_c}. \quad (4.14)$$

This is essentially the result of Bertolotti (1985) if $C \cos \psi_c$ is replaced by the scalar phase velocity of the two-dimensional Tollmien–Schlichting wave for which $\psi_c = 0$. For $C = 0$, i.e. the stationary crossflow vortices investigated in this paper, the one-term relation (4.14) reduces to Gaster's result. Bertolotti (1985) also gave the result corresponding to the two-term expansion in (4.13).

For the three different types of secondary instability modes in figure 16 the spatial growth rates $-a_{c,i}^{(s)}$ are compared with the corresponding temporal growth rates $\sigma_r^{(t)}$ in figure 19(a) as functions of the real wavenumber b_c . The spatial growth rates, depicted by the dash-dotted curves, were obtained by applying the approximate relation (4.14) with $C = 0$ (Gaster transformation). For this purpose the group velocity $c_{g,c}$ in the

chord direction, shown in figure 19(b), was computed numerically via finite differences. As can be seen, the group velocity is distinctly different for the three different mode types. Similarly to Gaster (1962) we had to assume that the growth rate is small in deriving the approximate relation (4.14). To check the accuracy of (4.14) in the Gaster limit $C = 0$ and in view of the cautioning remarks of Brevdo (1992a), we computed a few spatial results (marked by the symbols in figure 19) by solving the secondary instability equations (4.7), (4.8) for complex σ as well as complex wavenumbers a_p, b_p . In this local iteration we varied σ_r from $\sigma_r^{(l)}$ to $\sigma_r^{(s)}$ by keeping the spanwise wavelength, i.e. b_c , as well as the frequency in the laboratory system, i.e. $\sigma_i - Ca_{p,r}$, constant. The sample points show that Gaster's (1962) transformation is quite accurate also for the secondary instabilities of the stationary crossflow vortices in this example.

5. Conclusion and outlook

Motivated by the experimentally observed amplitude saturation before nonlinear breakdown we computed nonlinear equilibrium solutions for the DLR swept-plate experiment. Saturated stationary as well as travelling crossflow vortices were examined by means of a continuation procedure. In this local analysis the non-rational parallel-flow approximation in conjunction with the traditional 'force-term formulation' was found to lead to unphysical mean flow profiles at higher amplitudes. To remedy this to some extent Herbert's (1974) local similarity approximation for the streamwise variation of the mean flow distortion has been applied with considerably improved results. However, one has to keep in mind that for a rational treatment a non-local theory is necessary which at present is outside our computational capabilities.

To obtain an error estimate for applying the local similarity approximation we compared the equilibrium solutions with non-local, nonlinear parabolized stability equation (PSE) results. This led to the clarification of the bifurcation behaviour of the spatially oscillating states observed in PSE and critical layer theory results. The spatial bifurcation from the stationary equilibrium occurs close to the leading edge and the wavelength of the oscillatory solution is comparable to the chord length of the swept plate. The PSE results were found to depend strongly on the applied initial conditions, i.e. receptivity, and did not approach a unique saturated state as often assumed. Experimental results are usually depicted on a logarithmic scale where this variation of saturation amplitude can be overlooked easily. The amplitude of our nonlinear equilibrium solution seems to envelope the maximum amplitudes of the spatial PSE results as x_c/c increases. Taking advantage of this and in order to avoid the additional complication of receptivity we used the stationary, equilibrated crossflow vortices as the nonlinear model flow for an amplitude-dependent parameter study of temporal secondary instabilities.

In agreement with previous investigations we found that fairly high threshold amplitudes of the primary crossflow vortex are necessary to initiate the high-frequency secondary instability. For our equilibrium solutions the most amplified secondary instability mode is always of 'mode I' type, cf. Malik *et al.* (1996), which can be correlated with spanwise inflection points in the wake-like profile of the velocity along the vortex axis. With increasing downstream distance more and more unstable modes appear. The amplification and frequency of the most amplified mode increase substantially and the frequency is in the experimentally observed range. It can therefore be expected that this mode plays an important role in the breakdown process. Extending Gaster's (1962) transformation, which relates the spatial growth rate of primary instabilities to the temporal growth rate, to secondary instabilities it

is shown that this approximate relation is quite accurate for our stationary crossflow vortices.

At the same time it becomes clear that the high-frequency secondary instabilities only initiate the breakdown process. To prove the self-sustaining nature through nonlinear interactions, cf. Waleffe (1997), signalling a global bifurcation with a differing basin of attraction as postulated by Dauchot & Manneville (1997), remains a formidable task within a non-local theory. However, using the parallel-flow approximation, a locally valid absolute/convective stability analysis of the secondary instabilities considered above could give important clues for the existence of such a self-sustaining process and is at present under investigation. The equilibrium solutions computed above with x_c/c as parameter seem to be well suited for such an analysis. In analogy to the flow behind plane and axisymmetric blunt bodies, cf. Koch (1985) and Monkewitz (1988), the wake-like velocity profiles in the crossflow vortex make the existence of an absolute instability, i.e. a self-excited oscillation, of secondary instability modes quite plausible. As demonstrated by Delbende, Chomaz & Huerre (1998) or Olendraru *et al.* (1999), swirl in axisymmetric wakes promotes the onset of an absolute instability. In our case we have neither a plane nor an axisymmetric wake flow. The base flow for the secondary instabilities is truly three-dimensional. If it can be shown that for this base flow such a change from convectively unstable to absolutely unstable secondary modes occurs we conjecture the following scenario: the convectively unstable primary instability generates the necessary nonlinear amplitude for the activation of the absolutely unstable secondary instability with far-reaching consequences for transition control.

We are grateful to M. Kloker and G. Bonfigli for performing the spatial DNS computations in figure 7, and to V. Theofilis for stimulating discussions. Furthermore, we thank the reviewers for their helpful criticism and for pointing out some references which we had overlooked. The partial support of the Deutsche Forschungsgemeinschaft, Bonn–Bad Godesberg under the contract Ko 1722/2-1 is gratefully acknowledged.

Appendix. Secondary instability equation coefficients

With $n = \mu + \nu$ and using the abbreviations

$$\alpha_{\mu,\nu} = (n + \delta - \nu)\alpha_\psi, \quad \alpha_{\mu,0} = (n + \delta)\alpha_\psi, \quad \alpha_{0,\nu} = \nu\alpha_\psi,$$

$$k_{\mu,\nu} = \{(n + \delta - \nu)^2\alpha_\psi^2 + b_\psi^2\}^{1/2}, \quad k_{\mu,0} = \{(n + \delta)^2\alpha_\psi^2 + b_\psi^2\}^{1/2}$$

we obtain for the coefficients in the secondary instability equation (4.9):

$$A_{\mu,\nu}^{OS} = \begin{cases} -i\alpha_{\mu,0} \left[\frac{d^2 \hat{u}_{0,\nu}}{dy^2} + k_{\mu,0}^2 \hat{u}_{0,\nu} \right] - ib_\psi \left[\frac{d^2 \hat{w}_{0,\nu}}{dy^2} + k_{\mu,0}^2 \hat{w}_{0,\nu} \right], & \nu = 0 \\ \frac{1}{\alpha_{0,\nu}} \left[\alpha_{\mu,0} \frac{d^3 \hat{v}_\nu}{dy^3} + (\alpha_{\mu,\nu} - \alpha_{0,\nu}) k_{\mu,0}^2 \frac{d \hat{v}_\nu}{dy} \right] + \frac{b_\psi}{\alpha_{0,\nu}} \left[k_{\mu,0}^2 \hat{\eta}_\nu + \frac{d^2 \hat{\eta}_\nu}{dy^2} \right], & \nu \neq 0, \end{cases}$$

$$B_{\mu,\nu}^{OS} = \begin{cases} 0, & \nu = 0 \\ k_{\mu,0}^2 \left[\frac{\alpha_{0,\nu} \alpha_{\mu,\nu}}{k_{\mu,\nu}^2} - 1 \right] \hat{v}_\nu + \frac{b_\psi^2 - \alpha_{\mu,0} \alpha_{\mu,\nu}}{k_{\mu,\nu}^2} \frac{d^2 \hat{v}_\nu}{dy^2} - \frac{2b_\psi \alpha_{\mu,\nu}}{k_{\mu,\nu}^2} \frac{d \hat{\eta}_\nu}{dy}, & \nu \neq 0, \end{cases}$$

$$\begin{aligned}
C_{\mu,v}^{OS} &= \begin{cases} i[\alpha_{\mu,0}\hat{u}_{0,v} + b_\psi\hat{w}_{0,v}], & v = 0 \\ \frac{1}{\alpha_{0,v}} \left[\frac{2b_\psi^2\alpha_{0,v}}{k_{\mu,v}^2} - \alpha_{\mu,0} \right] \frac{d\hat{v}_v}{dy} - b_\psi \left[\frac{1}{\alpha_{0,v}} + \frac{2\alpha_{\mu,v}}{k_{\mu,v}^2} \right] \hat{\eta}_v, & v \neq 0, \end{cases} \\
D_{\mu,v}^{OS} &= \begin{cases} 0, & v = 0 \\ \left[1 + \frac{\alpha_{0,v}\alpha_{\mu,v}}{k_{\mu,v}^2} \right] \hat{v}_v, & v \neq 0, \end{cases} \\
E_{\mu,v}^{OS} &= \begin{cases} 0, & v = 0 \\ \frac{b_\psi}{k_{\mu,v}^2} \left[(\alpha_{\mu,v} + \alpha_{\mu,0}) \frac{d^2\hat{v}_v}{dy^2} - \alpha_{\mu,0}k_{\mu,v}^2\hat{v}_v + 2b_\psi \frac{d\hat{\eta}}{dy} \right], & v \neq 0, \end{cases} \\
F_{\mu,v}^{OS} &= \begin{cases} 0, & v = 0 \\ \frac{2b_\psi}{k_{\mu,v}^2} \left[\alpha_{\mu,v} \frac{d\hat{v}_v}{dy} + b_\psi\hat{\eta}_v \right], & v \neq 0, \end{cases} \quad G_{\mu,v}^{OS} = \begin{cases} 0, & v = 0 \\ -\frac{\alpha_{0,v}b_\psi}{k_{\mu,v}^2} \hat{v}_v, & v \neq 0. \end{cases}
\end{aligned}$$

Similarly, the coefficients in equation (4.10) are

$$\begin{aligned}
A_{\mu,v}^{SQ} &= \begin{cases} i \left[b_\psi \frac{d\hat{u}_{0,v}}{dy} - \alpha_{\mu,0} \frac{d\hat{w}_{0,v}}{dy} \right], & v = 0 \\ \frac{1}{\alpha_{0,v}} \left[\alpha_{\mu,0} \frac{d\hat{\eta}_v}{dy} - b_\psi \frac{d^2\hat{v}_v}{dy^2} \right], & v \neq 0, \end{cases} \\
B_{\mu,v}^{SQ} &= \begin{cases} 0, & v = 0 \\ -\frac{b_\psi^2 + \alpha_{\mu,0}\alpha_{\mu,v}}{k_{\mu,v}^2} \hat{\eta}_v, & v \neq 0, \end{cases} \quad C_{\mu,v}^{SQ} = \begin{cases} 0, & v = 0 \\ \frac{\alpha_{0,v}b_\psi}{k_{\mu,v}^2} \hat{v}_v, & v \neq 0, \end{cases} \\
D_{\mu,v}^{SQ} &= \begin{cases} i[\alpha_{\mu,0}\hat{u}_{0,v} + b_\psi\hat{w}_{0,v}], & v = 0 \\ -\frac{\alpha_{\mu,0}}{\alpha_{0,v}} \frac{d\hat{v}_v}{dy} + b_\psi \left[\frac{\alpha_{0,v}}{k_{\mu,v}^2} - \frac{1}{\alpha_{0,v}} \right] \hat{\eta}_v, & v \neq 0, \end{cases} \\
E_{\mu,v}^{SQ} &= \begin{cases} 0, & v = 0 \\ \frac{b_\psi^2 + \alpha_{\mu,0}\alpha_{\mu,v}}{k_{\mu,v}^2} \hat{v}_v, & v \neq 0. \end{cases}
\end{aligned}$$

REFERENCES

- ANDERSSON, P., BOTTARO, A., HENNINGSON, D. & LUCHINI, P. 1999 On the breakdown of boundary layer streaks. *J. Fluid Mech.* (submitted).
- ARNAL, D. 1992 Boundary layer transition: Prediction, application to drag reduction. In *AGARD Special Course on Skin Friction Drag Reduction*, AGARD-R-786, pp. 5.1–5.59.
- ARNAL, D., COUSTOLS, E. & JUILLEN, J. 1984 Experimental and theoretical study of transition phenomena on an infinite swept wing. *Rech. Aerosp.* (4), 275–290.
- BAKE, S., KACHANOV, Y. & FERNHOLZ, H. 1996 Subharmonic K-regime of boundary-layer breakdown. In *Transitional Boundary Layers in Aeronautics* (ed. R. A. W. M. Henkes & J. L. van Ingen), pp. 81–88. North-Holland.

- BALACHANDAR, S., STREETT, C. & MALIK, M. 1992 Secondary instability in a rotating disk flow. *J. Fluid Mech.* **242**, 323–347.
- BERLIN, S., WIEGEL, M. & HENNINGSON, D. 1999 Numerical and experimental investigations of oblique boundary layer transition. *J. Fluid Mech.* **393**, 23–57.
- BERTOLOTTI, F. 1985 Temporal and spatial growth of subharmonic disturbances in Falkner–Skan flows. Master's thesis, Virginia Polytechnic Institute.
- BERTOLOTTI, F. 1991 Linear and nonlinear stability of boundary layers with streamwise varying properties. PhD thesis, The Ohio State University.
- BERTOLOTTI, F. 1996 On the birth and evolution of disturbances in three-dimensional boundary layers. In *Proc. IUTAM Symp. on Nonlinear Instability and Transition in Three-Dimensional Boundary Layers* (ed. P. Duck & P. Hall), pp. 247–256. Kluwer.
- BERTOLOTTI, F., HERBERT, T. & SPALART, P. 1992 Linear and nonlinear stability of the Blasius boundary layer. *J. Fluid Mech.* **242**, 441–474.
- BIPPES, H. 1999 Basic experiments on transition in three-dimensional boundary layers dominated by crossflow instability. *Prog. Aero. Sci.* **35**, 363–412.
- BIPPES, H., MÜLLER, B. & WAGNER, M. 1991 Measurements and stability calculations of the disturbance growth in an unstable three-dimensional boundary layer. *Phys. Fluids A* **3**, 2371–2377.
- BONFIGLI, G. & KLOKER, M. 1999 Spatial Navier–Stokes simulation of crossflow-induced transition in a three-dimensional boundary layer. In *New Results in Numerical and Experimental Fluid Dynamics* (ed. W. Nitsche, H.-J. Heineman & R. Hilbig), pp. 61–68, Vieweg.
- BOTTARO, A. & KLINGMANN, B. 1996 On the linear breakdown of Görtler vortices. *Eur. J. Mech. B/Fluids* **15**, 301–330.
- BREUDO, L. 1992a A note on the Gaster transformation. *Z. Angew. Math. Mech.* **75**, 305–306.
- BREUDO, L. 1992b Spatially amplifying waves in plane Poiseuille flow. *Z. Angew. Math. Mech.* **72**, 163–174.
- BREUDO, L. & BRIDGES, T. 1996 Absolute and convective instabilities of spatially periodic flows. *Phil. Trans. R. Soc. Lond. A* **354**, 1027–1064.
- BRIDGES, T. & MORRIS, P. 1984 Differential eigenvalue problems in which the parameter appears nonlinearly. *J. Comput. Phys.* **55**, 437–460.
- BRIGGS, R. 1964 *Electron-Stream Interaction with Plasmas*. Research Monograph No. 29, MIT Press, Cambridge, Massachusetts.
- BROWN, S. & SMITH, F. 1996 On vortex/wave interactions. Part 1. Non-symmetrical input and cross-flow in boundary layers. *J. Fluid Mech.* **307**, 101–133.
- CANUTO, C., HUSSAINI, A., QUATERONI, A. & ZANG, T. 1987 *Spectral Methods in Fluid Dynamics* Springer.
- COPIE, M.-L. 1996 Stabilité linéaire et faiblement non linéaire d'une couche limite pour un fluide incompressible, avec l'approche PSE. PhD thesis, L'Ecole Nationale Supérieure de l'Aéronautique et de l'Espace.
- CORRAL, R. & JIMÉNEZ, J. 1992 Direct numerical simulations of the transitional 3D incompressible boundary layer. *Tech. Note ETSIA/MF-922*, Universidad Politécnica Madrid.
- DAUCHOT, O. & MANNEVILLE, P. 1997 Local versus global concepts in hydrodynamic stability theory. *J. Phys. II Paris* **7**, 371–389.
- DELBENDE, I., CHOMAZ, J.-M. & HUERRE, P. 1998 Absolute/convective instabilities in the Batchelor vortex: a numerical study of the linear impulse response. *J. Fluid Mech.* **355**, 229–254.
- DEYHLE, H. & BIPPES, H. 1996 Disturbance growth in an unstable three-dimensional boundary layer and its dependence on environmental conditions. *J. Fluid Mech.* **316**, 73–113.
- DEYHLE, H., HÖHLER, G. & BIPPES, H. 1993 Experimental investigation of instability wave propagation in a 3-D boundary-layer flow. *AIAA. J.* **31**, 637–645.
- ERLEBACHER, G. & HUSSAINI, M. 1990 Numerical experiments in supersonic boundary-layer stability. *Phys. Fluids A* **2**, 94–104.
- FISCHER, T. 1995 On the nonlinear development of disturbances in boundary layers assumed as parallel. *Eur. J. Mech. B/Fluids* **14**, 577–599.
- FISCHER, T. & DALLMANN, U. 1987 Theoretical investigation of secondary instability of three-dimensional boundary-layer flows. *AIAA Paper* 87–1338.
- FISCHER, T. & DALLMANN, U. 1991 Primary and secondary stability analysis of a three-dimensional boundary-layer flow. *Phys. Fluids A* **3**, 2378–2391.

- FISCHER, T., HEIN, S. & DALLMANN, U. 1993 A theoretical approach for describing secondary instability features in three-dimensional boundary-layer flows. *AIAA Paper* 93-0080.
- GAJJAR, J. 1996 On the nonlinear evolution of a stationary cross-flow vortex in a fully three-dimensional boundary layer flow. In *Proc. IUTAM Symp. on Nonlinear Instability and Transition in Three-Dimensional Boundary Layers, Manchester, UK* (ed. P. Duck & P. Hall), pp. 317-326. Kluwer.
- GASTER, M. 1962 A note on the relation between temporally increasing and spatially increasing disturbances in hydrodynamic stability. *J. Fluid Mech.* **14**, 222-224.
- GREGORY, N., STUART, J. & WALKER, W. 1955 On the stability of three-dimensional boundary layers with application to the flow due to a rotating disk. *Phil. Trans. R. Soc. A* **248**, 155-199.
- HALL, P. 1983 The linear development of Görtler vortices in growing boundary layers. *J. Fluid Mech.* **130**, 41-58.
- HEIN, S., BERTOLOTTI, F., SIMEN, M., HANIFI, A. & HENNINGSON, D. 1994 Linear nonlocal instability analysis – the linear NOLOT code –. DLR-IB 223-94 A56.
- HERBERT, T. 1974 Über endliche Amplituden periodischer Störungen der Grenzschicht an der ebenen Platte. *DLR Res. Rep.* DLR-FB 74-53.
- HERBERT, T. 1984 Secondary instability of shear flows. In *AGARD Special Course on Stability and Transition of Laminar Flow, AGARD-R-709*, pp. 7.1-7.13.
- HERBERT, T. 1988 Secondary instability of boundary layers. *Ann. Rev. Fluid Mech.* **20**, 487-526.
- HERBERT, T. 1997 Parabolized stability equations. *Ann. Rev. Fluid Mech.* **29**, 245-283.
- HERBERT, T. & MORKOVIN, M. 1980 Dialogue on bridging some gaps in stability and transition research. In *IUTAM Symp. on Laminar-Turbulent Transition* (ed. R. Eppler & H. Fasel), pp. 47-72. Springer.
- HÖGBERG, M. & HENNINGSON, D. 1998 Secondary instability of cross-flow vortices in Falkner-Skan-Cooke boundary layers. *J. Fluid Mech.* **368**, 339-357.
- HOLMES, P., LUMLEY, J. & BERKOOZ, G. 1996 *Turbulence, Coherent Structures, Dynamical Systems and Symmetry*. Cambridge University Press.
- JANKE, E. 1998 Nonlinear stability and control of three-dimensional boundary layers. PhD thesis, Old Dominion University.
- JANKE, E. & BALAKUMAR, P. 1998a Nonlinear stability of three-dimensional boundary layers. *AIAA Paper* 98-0337.
- JANKE, E. & BALAKUMAR, P. 1998b On the secondary instability of three-dimensional boundary layers. *Theor. Comput. Fluid Dyn.* (submitted).
- JOSLIN, R. & STRETT, C. 1994 The role of stationary cross-flow vortices in boundary-layer transition on swept wings. *Phys. Fluids* **6**, 3442-3453.
- KAWAKAMI, M., KOHAMA, Y. & OKUTSU, M. 1999 Stability characteristics of stationary crossflow vortices in three-dimensional boundary layer. *AIAA Paper* 99-0811.
- KEEFE, L. 1993 Drag reduction in channel flow using nonlinear control. *AIAA Paper* 93-3279.
- KELLER, H. 1977 Numerical solution of bifurcation and nonlinear eigenvalue problems. In *Applications of Bifurcation Theory* (ed. P. H. Rabinowitz), pp. 359-384. Academic Press.
- KLEBANOFF, P., TIDSTROM, K. & SARGENT, L. 1962 The three-dimensional nature of boundary-layer instability. *J. Fluid Mech.* **12**, 1-39.
- KLEISER, L. & ZANG, T. 1991 Numerical simulation of transition in wall-bounded shear flows. *Ann. Rev. Fluid Mech.* **23**, 495-537.
- KOCH, W. 1985 Local instability characteristics and frequency determination of self-excited wake flows. *J. Sound Vib.* **99**, 53-83.
- KOCH, W. 1992 On a degeneracy of temporal secondary instability modes in Blasius boundary-layer flow. *J. Fluid Mech.* **243**, 319-351.
- KOCH, W. 1996 Nonlinear crossflow saturation in three-dimensional boundary layers. In *Proc. IUTAM Symp. on Nonlinear Instability and Transition in Three-Dimensional Boundary Layers, Manchester, UK* (ed. P. Duck & P. Hall), pp. 299-308. Kluwer.
- KOHAMA, Y. 1984 Study on boundary layer transition of a rotating disk flow. *Acta Mechanica* **50**, 193-199.
- KOHAMA, Y. 1987 Cross-flow instability in rotating disk boundary layer. *AIAA Paper* 87-1340.
- KOHAMA, Y., ONONDERA, T. & EGAMI, Y. 1996 Design and control of crossflow instability field. In *Proc. IUTAM Symp. on Nonlinear Instability and Transition in Three-Dimensional Boundary Layers, Manchester, UK* (ed. P. Duck & P. Hall), pp. 147-156. Kluwer.

- KOHAMA, Y., SARIC, W. & HOOS, W. 1991 A high-frequency, secondary instability of crossflow vortices, that leads to transition. In *Proc. RAS Conf. on Boundary-Layer and Control, Cambridge, UK*, pp. 4.1–4.13.
- LERCHE, T. 1997 Experimentelle Untersuchung nichtlinearer Strukturbildung im Transitionsprozess einer instabilen dreidimensionalen Grenzschicht. *Fortschritt-Bericht VDI Reihe 7*, no 310. VDI-Verlag Düsseldorf (Germany).
- LI, F. & MALIK, M. 1995 Fundamental and subharmonic secondary instability of Görtler vortices. *J. Fluid Mech.* **297**, 77–100.
- LINGWOOD, R. 1995 Absolute instability of the boundary layer on a rotating disk. *J. Fluid Mech.* **299**, 17–33.
- LINGWOOD, R. 1996 An experimental study of absolute instability of the rotating-disk boundary-layer flow. *J. Fluid Mech.* **314**, 373–405.
- LINGWOOD, R. 1997 On the impulse response for swept boundary-layer flows. *J. Fluid Mech.* **344**, 317–334.
- MALIK, M. 1986 Numerical simulation of transition in a three-dimensional boundary layer. In *Proc. Tenth Intl Conf. on Numerical Methods in Fluid Dynamics* (ed. F. G. Zhuang & T. L. Zhu), pp. 457–461. Springer.
- MALIK, M. 1997 Boundary-layer transition prediction toolkit. *AIAA Paper 97–1904*.
- MALIK, M. & LI, F. 1992 Three-dimensional boundary layer stability and transition. *SAE Paper 921991*.
- MALIK, M. & LI, F. 1993 Transition studies for swept wing flows using PSE. *AIAA Paper 93–0077*.
- MALIK, M., LI, F. & CHANG, C.-L. 1994 Crossflow disturbances in three-dimensional boundary layers: nonlinear development, wave interaction and secondary instability. *J. Fluid Mech.* **268**, 1–36.
- MALIK, M., LI, F. & CHANG, C.-L. 1996 Nonlinear crossflow disturbances and secondary instabilities in swept-wing boundary layers. In *Proc. IUTAM Symp. on Nonlinear Instability and Transition in Three-Dimensional Boundary Layers, Manchester, UK* (ed. P. Duck & P. Hall), pp. 257–266. Kluwer.
- MALIK, M., WILKINSON, S. & ORSZAG, S. 1981 Instability and transition in rotating disk flow. *AIAA Paper 81–4225*.
- MEYER, F. 1989 Numerische Simulation der Transition in dreidimensionalen Grenzschichten. *DLR Res. Rep.* DLR-FB 89-12, Universität Karlsruhe.
- MEYER, F. & KLEISER, L. 1988 Numerical investigation of transition in 3D boundary layers. In *AGARD Conf. on Fluid Dynamics of Three-Dimensional Turbulent Shear Flows and Transition, AGARD-R-438*, pp. 16.1–16.17.
- MICHEL, J., ARNAL, D. & JUILLEN, J. 1985 Experimental and theoretical studies of boundary layer transition on a swept infinite wing. In *IUTAM Symp. on Laminar–Turbulent Transition* (ed. V. V. Kozlov), pp. 553–561. Springer.
- MILINAZZO, F. & SAFFMAN, P. 1985 Finite-amplitude steady waves in plane viscous shear flows. *J. Fluid Mech.* **160**, 281–295.
- MONKEWITZ, P. 1988 A note on vortex shedding from axisymmetric bluff bodies. *J. Fluid Mech.* **192**, 561–575.
- MÜLLER, B. & BIPPES, H. 1988 Experimental study of instability modes in a three-dimensional boundary layer. In *AGARD Conf. on Fluid Dynamics of Three-Dimensional Turbulent Shear Flows and Transition, AGARD-R-438*, pp. 13.1–16.15.
- MÜLLER, W. 1995 Numerische Untersuchung räumlicher Umschlagvorgänge in dreidimensionalen Grenzschichtströmungen. PhD thesis, Universität Stuttgart.
- MÜLLER, W., BESTEK, H. & FASEL, H. 1995 Spatial direct numerical simulation of transition in a three-dimensional boundary layer. In *IUTAM Symp. on Laminar–Turbulent Transition* (ed. R. Kobayashi), pp. 397–404. Springer.
- NAYAR, N. & ORTEGA, J. 1993 Computation of selected eigenvalues of generalized eigenvalue problems. *J. Comput. Phys.* **108**, 8–14.
- NAYFEH, A. & PADHYE, A. 1979 Relation between temporal and spatial stability in three-dimensional flows. *AIAA J.* **17**, 1084–1090.
- NISHIOKA, M., ASAI, M. & IIDA, S. 1980 An experimental investigation of the secondary instability. In *IUTAM Symp. on Laminar–Turbulent Transition* (ed. R. Eppler & H. Fasel), pp. 37–46. Springer.

- NITSCHKE-KOWSKY, P. & BIPPES, H. 1988 Instability and transition of a three-dimensional boundary layer on a swept plate. *Phys. Fluids* **31**, 786–795.
- OLENDRARU, C., SELIER, A., ROSSI, M. & HUERRE, P. 1999 Inviscid instability of the Batchelor vortex: Absolute-convective transition and spatial branches. *Phys. Fluids* **11**, 1805–1820.
- PARK, D. & HUERRE, P. 1995 Primary and secondary instabilities of the asymptotic suction boundary layer on a curved plate. *J. Fluid Mech.* **283**, 249–272.
- POLL, D. 1985 Some observations of the transition process on the windward face of a long yawed cylinder. *J. Fluid Mech.* **150**, 329–356.
- REED, H. 1984 Wave interactions in swept-wing flows. *AIAA Paper* 84–1678.
- REED, H. 1988 Wave interactions in swept-wing flows. *Phys. Fluids* **30**, 3419–3426.
- REED, H. & SARIC, W. 1989 Stability of three-dimensional boundary layers. *Ann. Rev. Fluid Mech.* **21**, 235–284.
- REED, H., SARIC, W. & ARNAL, D. 1996 Linear stability theory applied to boundary layers. *Ann. Rev. Fluid Mech.* **28**, 389–428.
- SAAD, Y. 1992 *Numerical Methods for Large Eigenvalue Problems*. Manchester University Press.
- SARIC, W. 1992 Laminar-turbulent transition: fundamentals. In *AGARD Special Course on Skin Friction Drag Reduction*, AGARD-R-786, pp. 4.1–4.32.
- SEYDEL, R. 1994 *Practical Bifurcation and Stability Analysis From Equilibrium to Chaos*, 2nd edn. Springer.
- SMITH, F., BROWN, S. & BROWN, P. 1993 Initiation of three-dimensional nonlinear transition paths from an inflectional profile. *Eur. J. Mech. B/Fluids* **12**, 447–473.
- STOLTE, A. 1999 Investigation of transition scenarios in boundary-layer flows. PhD thesis, Georg-August-Universität Göttingen.
- TANI, I. 1980 Some thoughts on boundary layer transition. In *IUTAM Symp. on Laminar-Turbulent Transition* (ed. R. Eppler & H. Fasel), pp. 263–276. Springer.
- TAYLOR, M. & PEAKE, N. 1998 The long-time behaviour of incompressible swept wing boundary layers subject to impulsive forcing. *J. Fluid Mech.* **355**, 359–381.
- TURKYILMAZOGLU, M. & GAJJAR, J. 1999 On the absolute instability of the attachment-line and swept-Hiemenz boundary layers. *Theor. Comput. Fluid Dyn.* **13**, 57–75.
- WAGNER, M. 1992 Numerische Untersuchungen zum laminar-turbulenten Übergang in zwei- und dreidimensionalen Grenzschichten. *DLR Res. Rep.* DLR-FB 92-36.
- WALEFFE, F. 1997 On a self-sustaining process in shear flows. *Phys. Fluids* **9**, 883–900.
- WANG, M., HERBERT, T. & STUCKERT, G. 1994 Crossflow-induced transition in compressible swept-wing flows. *AIAA Paper* 94–2374.
- WHITE, F. 1974 *Viscous Fluid Flow*. McGraw-Hill.
- WIEGEL, M. 1997 Experimentelle Untersuchung von kontrolliert angeregten dreidimensionalen Wellen in einer Blasius-Grenzschicht. *Fortschritt-Bericht VDI Reihe 7*, no 312. VDI-Verlag Düsseldorf (Germany).
- WINTERGERSTE, T. & KLEISER, L. 1997 Breakdown of a crossflow vortex in a three-dimensional boundary layer. In *Direct and Large-Eddy Simulation II* (ed. J.-P. Chollet *et al.*), pp. 179–190. Kluwer.
- WRAY, A. & HUSSAINI, M. 1984 Numerical experiments in boundary-layer stability. *Proc. R. Soc. Lond. A* **392**, 373–389.
- ZURMÜHL, R. 1961 *Matrizen und ihre Technischen Anwendungen*, 3rd edn. Springer.